

2020-02-15

Quantifying the transient landscape response to active faulting using fluvial geomorphic analysis in the Qianhe Graben on the southwest margin of Ordos, China

Liu, Z

<http://hdl.handle.net/10026.1/15175>

10.1016/j.geomorph.2019.106974

Geomorphology

Elsevier

All content in PEARL is protected by copyright law. Author manuscripts are made available in accordance with publisher policies. Please cite only the published version using the details provided on the item record or document. In the absence of an open licence (e.g. Creative Commons), permissions for further reuse of content should be sought from the publisher or author.

1 *NOTICE: this is the author's version of a work that was accepted for publication in*
2 *Geomorphology. Changes resulting from the publishing process, such as peer review, editing,*
3 *corrections, structural formatting, and other quality control mechanisms may not be reflected*
4 *in this document. Changes may have been made to this work since it was submitted for*
5 *publication.*

6

7 **Quantifying the transient landscape response to active faulting using fluvial**
8 **geomorphic analysis in the Qianhe Graben on the southwest margin of Ordos,**
9 **China**

10

11 Zhiheng Liu^{a,b}, Ling Han^{a,*}, Sarah J. Boulton^b, Tingting Wu^a, Jianhua Guo^c

12

13 ^a School of Geology Engineering and Geomatics, Chang'an University, Xi'an 710064,
14 China

15 ^b School of Geography, Earth and Environmental Sciences, University of Plymouth,
16 Plymouth PL4 8AA, UK

17 ^c School of Electrical and Information Engineering, Tianjin University, Tianjin 300072,
18 China

19

20 * Correspondence to: hanling@chd.edu.cn (Ling Han)

21

22 **ABSTRACT:**

23 River morphology has been widely used to record and track the transient landscape
24 response to active faulting. Here we evaluate the landscape response to active faulting
25 in the Qianhe Graben of southwest Ordos, China. In this region, it has been difficult to
26 determine the activity of mapped faults because of the presence of thick Quaternary
27 Loess; however, by analysing the presence and distribution of slope-break knickpoints
28 in river longitudinal profiles, the ongoing tectonic uplift of the Qianhe Graben can be
29 investigated. The alignment of vertical-step knickpoints gives a new insight into the
30 location of an active fault on the southern margin of Qianhe Graben. Additionally,
31 slope-break knickpoints, typical of fault controlled landscape change, were identified
32 from 24 river longitudinal profiles that drain across normal faults along both graben
33 margins. Along strike from north to south, the knickpoints varied systematically with
34 relief, and the height of the knickpoints also decrease to the southeast. Indicating that
35 the rate of motion on the faults, likely is greater in the northwest and decays
36 southeastwards. The horizontal knickpoint retreat rates range from 0.3 - 27.3 mm/yr,
37 constraining the landscape response time with fault initiation at 1.2 ~ 1.4 Myr. In
38 comparison with other studies, the knickpoint recession triggered by base-level fall as
39 a result of faulting is relatively lower than when the base-level fall is the result of sea-
40 level fall potentially the result of different mechanism of retreat. Finally, the potential
41 for earthquakes along the Taoyuan-Guichuansi Fault (TGF) before and after fault
42 linkage was assessed, indicating the potential for earthquakes of M_w of 6.3 - 6.7 and

43 6.8 - 7.0, respectively. These observations not only suggest the knickpoints are
44 recording fault evolution in Qianhe Graben, but also provide information on seismic
45 hazard in this populous region.

46

47 **KEYWORDS:** Qianhe Graben; knickpoint; active faulting; transient landform response

48

49 **1 Introduction**

50 Tectonic geomorphology is the investigation of the interaction between active tectonics
51 and surface processes, reflecting the coupling relationship between deep geophysical
52 structures and climate processes. Tectonic geomorphic landforms record the
53 landscape response to the spatial distribution of active faults (Kirby et al., 2003;
54 Boulton and Whittaker, 2009; Kirby and Ouimet, 2011; Ozkaymak and Sözbilir, 2012;
55 Hergarten et al., 2016; Topal et al., 2016; Dong et al., 2017; Owen et al., 2017). In
56 bedrock fluvial systems, rivers are sensitive to changes in boundary conditions, such
57 as structure, climate and lithology (Kirby et al., 2003; Whittaker, 2012; Whittaker and
58 Boulton, 2012; Allen et al., 2013; Cyr et al., 2014), and transmit the signal of tectonic
59 and climatic change to the surrounding landscape by setting the landscape response
60 time (Whipple and Tucker, 1999; Kirby et al., 2003). Furthermore, rivers are an
61 effective way to track neo-tectonic movement and topographic evolution (Whipple and
62 Tucker, 1999; Jiang et al., 2016). Previous studies have demonstrated that fluvial
63 geomorphologic parameters can record uplift rates, give insights into active faults, and
64 quantitatively study the external morphological characteristics formed by the internal
65 dynamic geological process (e.g., Whipple and Meade, 2006; Whipple, 2009;
66 Castellort et al., 2012; Kirby and Whipple, 2012; Boulton et al., 2014; Schanz and
67 Montgomery, 2016; Kent et al., 2017). As a result, fluvial morphologic indices of river
68 longitudinal profiles have become a widespread and easily implemented method to
69 study faulting in active tectonic regions, characterised by transient landscapes
70 responding to boundary condition perturbation (Whipple, 2002; Whittaker et al., 2008;

71 Ozkaymak and Sözbilir, 2012; Whittaker and Boulton, 2012; Faghih et al., 2015; Yan
72 et al., 2015; Matoš et al., 2016; Topal et al., 2016; Tepe and Sözbilir, 2017).

73

74 In some locations, owing to the existence of various limitations, such as thick
75 Quaternary sequences or physical (in)accessibility, it can be difficult to directly
76 measure the slip rate of faults. For example, the Qianhe Graben is a Cenozoic faulted
77 basin covered by thick extensional/transensional deposits of Quaternary loess (~ 100
78 - 120 m thick) (Fan et al, 2016), located at the intersection of the Liupanshan Fault
79 (LPSF) and Qinling Fault (KLF) in China (Fan et al., 2018; Zhang et al., 2019) (Fig.
80 1b). The thick loess and high relief make the area difficult to explore in the field, and
81 most recent research has focused on applying traditional methods (e.g., hypsometric
82 integral, stream length-gradient index, valley floor width-to-height ratio) (Chen et al.,
83 2003; Cheng et al., 2018; Zhang et al., 2019) to reveal the geomorphic effect of the
84 faults. However, such methods cannot constrain rates of faulting or the rate of
85 landscape response to changing base level. To address this challenge, stream profile
86 analysis offers an alternative method to investigate neotectonic deformation, and the
87 growth and linkage of faults of the study area (Kirby et al., 2003; Wobus et al., 2006;
88 Boulton and Whittaker, 2009; Kirby and Whipple, 2012; Boulton et al., 2014; Kent et
89 al., 2017). In transient landscapes, knickpoint (the point in the long profile where the
90 rate of change of channel gradient reaches local maximum) (Haviv et al., 2010;
91 Whittaker and Boulton, 2012; Kent et al., 2016) characteristics and normalized channel
92 steepness (k_{sn}) can be used to investigate fault slip rate and rock uplift rate by

93 analysing digital elevation models (DEMs) (Snyder et al., 2000; Bishop et al., 2005;
94 Crosby and Whipple, 2006; Castillo et al., 2014; Castillo, 2017; Gailleton et al., 2019;
95 Robustelli, 2019). Therefore, in the absence of direct geodetic constraints in active
96 settings much information can be gained through the investigation of knickpoint
97 characteristics, giving new insights into active faulting.

98

99 In this study, the fluvial morphologic indices of longitudinal profiles in Qianhe Graben
100 are extracted to investigate the landscape response to active faults based on digital
101 elevation model (DEM) and GIS spatial analyses. Specifically, the main purposes of
102 this study are: (1) to investigate the topographic response to active faulting by
103 identifying the styles of knickpoints from river longitudinal profiles; (2) to quantify the
104 transient fluvial landscape response to active faulting in this area; (3) to evaluate
105 present and future earthquake hazard in the study area.

106

107 **2 Geological background**

108 The Qianhe Graben is the westernmost extent of the Weihe Graben, located at the
109 intersection between the southwest margin of the Ordos block, the southeastern
110 Liupan-Longxi Plateau, and the northern Qinling fold system (Fig. 1). The palaeo-
111 surface of the study area is buried by Quaternary loess, 100 - 120 m thick (Fan et al.,
112 2016), but bedrock sedimentary strata are exposed dating from the Precambrian to
113 Neogene. The graben is defined by a number of active faults (Wang et al., 2011; Li et
114 al., 2013; Guo et al., 2016; Dong et al., 2017; Chen et al., 2018b; Cheng et al., 2018;

115 Zhang et al., 2019), with four main NW-SE trending active faults; the Taoyuan-
116 Guchuansi Fault (TGF), the Guguan-Guozhen Fault, (GGF), the Qianyang-Biaojiao
117 Fault (QBF), and the Qishan-Mazhao Fault (QMF), and the minor fault Qinling Fault
118 (QLF) (Fig. 1c).

119

120 Previous studies have shown that earthquakes occur frequently in the study area (Fan
121 et al., 2018), and the possibility of large earthquakes ($> M_w 6.0$) is high (Cheng et al.,
122 2014). However, according to the existing seismicity data (Fig. 1c), the earthquakes
123 that have affected the region during the instrumental period (from 1990 to present) are
124 smaller, $< M_w 5.5$, while most are $\leq M_w 2.0$. Even the 1556 Huaxian earthquake (M_w
125 8.5) and 1704 Longxian earthquake ($M_w 6.0$) (Fig. 1a, b), which occurred relatively
126 close to the study area, were over 300 years ago (Cheng et al., 2014; Hou et al., 1998).
127 Little information exists on the rates of fault slip. However, since 1.2 ~ 1.4 Ma, the
128 Quaternary activity with average slip rate on the QMF has been estimated, through a
129 combination of palaeoseismology, geomorphology, and deformation survey, as ~ 0.03
130 - 1.50 mm/yr, while GGF slip rate is ~ 0.03 mm/yr (Shi, 2011; Lin et al., 2015). Along
131 the southern margin of the Ordos block, fault activity has increased since 5 Ma owing
132 to the rapid uplift (2.94 ± 0.15 mm/yr) of the Qinling Mountains (Li et al., 2012) and
133 rifting of the Weihe Basin (Ren et al., 2015).

134

135 The active faults bound regions of distinct bedrock lithology. More than 50% of the
136 study area is Quaternary loess (Fig. 1c). To the north of the QMF, the bedrock is

137 composed of red sandstone and conglomerate forming the southwest margin of Ordos
138 block. These sedimentary rocks were deposited during the Jurassic to Cretaceous (Li
139 et al., 2013) and are exposed in river valleys that have incised through the overlying
140 loess. To the east of the GGF are Neogene, Ordovician and Cambrian marbles and
141 limestones, which were exposed by the extrusion of the Longxi block (Fan et al., 2003;
142 Lin et al., 2011; Liang et al., 2014), and to the west of GGF, there are outcrops of
143 Cretaceous conglomerates and sandstone. By contrast, to the west of TGF is a large
144 area of late Paleozoic and post-Triassic red granite (Fig. 1c).

145

146 In addition, there are distinct geomorphic regions within the study area controlled by
147 fault location and behaviour. Across the study area, the topography gradually
148 decreases in elevation from northwest to southeast (Fig. 2a). The highest points in the
149 northwest are composed of lower Paleozoic metamorphic rocks and Paleozoic
150 intermediate-acid intrusive rocks at altitudes of 1800 - 2200 m. The neotectonic uplift
151 driving topographic evolution has resulted in deep valleys and the steep ridges, which
152 form the watershed of the Weihe tributaries. By contrast, the low relief landscape of
153 the southeast gradually merges into the Weihe basin at an altitude of 600 - 700 m (Fig.
154 2a).

155 Since the late Cenozoic, in the Qianhe fault zone between the QMF and the QBF, five
156 asymmetric river terrace levels have developed along the Qianhe River (Sun, 2005;
157 Chen et al., 2018b) (Fig. 2a). Each terrace is composed of alluvial deposits and

158 covered by loess deposits, but the isochrones of paleosol sequences can be
159 accurately recognized (Zhang et al., 2019). The age of the terraces was determined
160 by magnetostratigraphic dating and field work (Chen et al., 2018b; Zhang et al. 2019),
161 providing ages for each terrace (T1 to T5): 0.01, 0.01 - 0.13, 0.12 - 0.60, 0.62 - 0.82,
162 and 1.2 - 1.4 Myrs, respectively (Li, 1991; Fan et al., 2018; Zhang et al., 2019).
163 Therefore, the oldest terrace provides a minimum age for the development of the
164 graben.

165

166 As shown in Figs. 2b, c, and d, three 100 km long strip profiles (AA', BB', CC')
167 perpendicular to the Qianhe fault zone were selected from northwest to southeast for
168 topographic and geomorphologic analysis of the Qianhe basin. It is clear that the TGF
169 and QMF faults are controlling the topography and form the major basin bounding
170 faults of Qianhe basin, which exhibits a basin and range-type topography. Under the
171 interaction of the four faults, the uplifted horsts and adjacent grabens, form the tectonic
172 structure of the region (Fig. 2e). Therefore, it is expected that the morphology of the
173 rivers crossing the Qianhe Graben will record evidence of river evolution and tectonic
174 uplift, providing a dataset for the study of the active faults.

175

176 **3 Method and data collection**

177 That stream profiles can provide insights to tectonic uplift has been confirmed for many
178 years (Hack, 1973; Howard and Kerby, 1983). Rivers in areas of active faulting not
179 only modify their topography to the regional base-level but also set boundary

180 conditions for the erosion and evolution of adjacent hillslopes (Castillo et al., 2017).
181 Therefore, a simple and efficient method of using river geomorphology to describe
182 bedrock channel forms and processes can reveal much information on the underlying
183 physical processes.

184

185 **3.1 River erosion model**

186 In order to analyze the fluvial geomorphic response of rivers to tectonic uplift in the
187 study area, a power law function of drainage area A and river channel slope S is used
188 as follows (Howard and Kerby, 1983; Whipple and Tucker, 1999; Kirby and Whipple,
189 2001; Bishop et al., 2005; Berlin and Anderson, 2007; Castillo et al., 2017; Scherler et
190 al., 2017):

$$E = K \times A^m \times S^n \quad (1)$$

191 Where E is the detachment-limited rate of bedrock channel erosion; K is erosion
192 coefficient related to lithologies, active faults, base level and climate; m and n are
193 constants.

194

195 In steady-state landscape, where the erosion equals uplift, the channel gradient can
196 be solved by Equation 1 for slope giving Equation 2:

$$S = \left(\frac{U}{K}\right)^{\frac{1}{n}} A^{-\frac{m}{n}} \quad (2)$$

197 Where m/n represents the concavity, U is uplift rate, and the coefficient $(U/K)^{1/n}$
198 represents the steepness.

199

200 To facilitate this calculation, the river hydraulic erosion model deduced from Equation
201 2 has been formed and widely used, along with the analysis of stream gradient and
202 drainage area, in the study of tectonic geomorphology (Hack, 1973; Howard et al.,
203 1994; Whipple, 2004; Boulton and Whittaker, 2009; Allen et al., 2013; Regalla et al.,
204 2013; Kale et al., 2014; Nexer et al., 2015; Kent et al., 2017; Sembroni and Molin,
205 2018), thus:

$$S = k_s A^{-\theta} \quad (3)$$

$$k_s = \left(\frac{U}{K}\right)^{\frac{1}{n}} \quad (4)$$

$$\theta = \frac{m}{n} \quad (5)$$

206 Where θ is the concavity index, and k_s is the steepness index.

207

208 The θ describes the rate of change of local channel slope and is generally between
209 0.3 and 0.6 in steady-state rivers (Hack, 1973). Changes in k_s can be used to
210 investigate the uplift rate if there is no significant lithologic variation and sediment
211 erosion (Snyder et al., 2000; Kirby and Whipple, 2012; Xue et al., 2018). Both k_s and
212 θ can be obtained by a linear regression from log-log slope-drainage area plots for
213 study rivers.

214

215 In such analyses, it has become an accepted approach to calculate a normalized
216 steepness index (k_{sn}) by using a reference θ , to avoid the strong correlation of k_s and

217 θ (Kirby and Whipple, 2012; Azañón et al., 2015). Generally, 0.45 is chosen as the
218 reference concavity index θ_{ref} . Therefore, the Equation 3 can be reformed as follows:

$$S = k_{sn} A^{-\theta_{ref}} \quad (6)$$

219

220 Not all rivers are in 'steady-state', and river longitudinal profiles can exhibit slope
221 discontinuities (knickpoints). A knickpoint is evidence of the transient state of the river,
222 and divides the channel into two parts with different steepness. Depending on the
223 shape of the knickpoints on a SA plot (Fig. 3), they can be divided into vertical-step
224 type knickpoints and slope-break type knickpoints (Wobus et al., 2006; Haviv et al.,
225 2010; Kirby and Whipple, 2012). A slope-break knickpoint separates downstream
226 incision from the upstream channel yet to respond to changes in boundary conditions.
227 It has been found that when such knickpoints are produced by a singular base-level
228 fall, knickpoints move at the same retrogression rate proportional to the upstream area,
229 causing the knickpoints of different rivers to be at the same altitude (Crosby and
230 Whipple, 2006; Berlin and Anderson, 2007). By contrast, the elevation of knickpoints
231 can scale with fault slip rate on a bounding faults, where multiple river cross a single
232 structure (Boulton and Whittaker, 2009; Whittaker and Boulton, 2012).

233

234 Generally, a vertical-step knickpoint is related to a change bedrock strength, which
235 appears at a lithologic boundary, fault zone or densely jointed zone, and the possibility
236 of migration to upstream is limited (Whipple et al., 2013; Wang et al., 2015). Although
237 the knickpoints formed by lithologic differences are generally considered fixed, the

238 channel is also divided into upper and lower parts, but there is little to no variation in
239 k_{sn} across the knickpoints.

240

241 Therefore, vertical-step knickpoints may have limited tectonic significance, while
242 slope-break knickpoints can represent local uplift caused by enhanced tectonic
243 movement (Fig. 3c and d), such as the initiation of faulting or an increase in slip on a
244 fault. Therefore, knickpoint analysis is a useful way to locate structures and analyse
245 geomorphologic evolution (Harkins et al., 2007; Boulton and Whittaker, 2009; Wang et
246 al., 2015; Chen et al., 2018a).

247

248 **3.2 River longitudinal profile**

249 In the absence of knickpoints, it has been proposed that further information on
250 boundary processes can be gained from the shape of the longitudinal profile (Chen et
251 al., 2006; Dong et al., 2017). Steady-state conditions require that uplift = erosion and
252 as a result the elevation of the bedrock channel is invariant. However, if the uplift rate
253 is not equal to the river erosion rate, the steady-state will be broken by the increase in
254 one of the two rates. If the uplift rate is higher, and the river elevation increases along
255 longitudinal profile with respect to time ($dz/dt > 0$) then the linear relationship will
256 transform into concave downward curve (Fig. 4a). By contrast, there will be an upward
257 concave curve when uplift rate < erosion (Chen et al., 2006). Based on Equation 3
258 above, we obtain logarithms on both sides as follows:

$$\log (S) = -\theta \times \log (A) + \log (k_s) \quad (7)$$

259

260 For steady-state profiles, the $\log(S)$ curve is in a straight line. Then, the $\log(S)$ curve
261 is convex when the uplift rate is greater. By contrast, the curve tends to be concave
262 (Fig. 4a), where uplift rates are lower.

263

264 According to the results of previous studies (e.g., Ohmori, 1991; Chen et al., 2003;
265 Rădoane et al., 2003), the shape of the river profiles can also be categorized. The
266 elevation Y of river longitudinal profile changes with the length X , and the profile can
267 be categorised as linear, exponential, logarithmic or power function type related to
268 different stages of landscape evolution (Chen et al., 2006; Dong et al., 2017) (Fig. 4b):

269 (1) Following surface uplift in tectonically active areas, the concavity of river
270 longitudinal profile can expressed as linear distribution ($Y=a-bX$);

271 (2) Where river incision is high, material is eroded from the upper and middle
272 reaches and transported to the lower reaches where sediment accumulates. As
273 a result, the curvature of the upper and middle reaches becomes larger,
274 gradually developing an exponential form ($Y=ae^{bX}$);

275 (3) Continuing erosion and deposition can further accentuate the profile curvature
276 resulting in a transition to the logarithmic profile-type ($Y=a\log X+b$);

277 (4) Under the influence of regional climate, bedrock fracture and other factors,
278 loose sediment is difficult to retain, the river erosion reaches a maximum, and
279 the concavity of longitudinal profile evolves into a power function ($Y=aX^b$).

280

281 In summary, the use of the geometric changes in the steady-state river longitudinal
282 profile can provide additional insights into the geomorphological evolution of a region
283 and provide a deeper understanding of the regional tectonic uplift in the absence of
284 knickpoints.

285

286 **3.3 Data collection**

287 The digital elevation model (DEM) data used here is the Shuttle Radar Topography
288 Mission (SRTM) DEM, which spans the 60°N to 56°S regions of the Earth's surface
289 from a radar topographic survey carried out jointly by National Aeronautics and Space
290 Administration (NASA) and National Imagery and Mapping Agency (NIMA), USA
291 (Hancock et al., 2006). This dataset covers 80% of the land surface, and the DEM is
292 provided as SRTM1 (1"× 1") and SRTM3 (3"× 3") data types, corresponding to the grid
293 resolution of 30 and 90 *m*, respectively. Fortunately, free access to the 1 arc sec data
294 is now available for the research area through the USGS Earth Explorer interface
295 (<https://earthexplorer.usgs.gov>). Previous research results have shown that SRTM
296 can be used in river hydrological analysis and is superior to ASTER-GDEM (Farr et al.,
297 2007; Arrowsmith and Zielke, 2009; Kirby and Whipple, 2012; Boulton and Stokes,
298 2018; Wang et al., 2018b). ArcGIS 10.2 software was used to reproject the DEM into
299 WGS_1984_UTM_Zone_48N, convert DEM data, splicing, filling holes, etc., to
300 produce the final DEM of Qianhe Graben (Fig. 2a).

301

302 The horizontal and vertical accuracy of the STRM DEM is > 99 % (Dong et al., 2017;
303 Farr et al., 2007), which has not limited the interpretation of tectonic landforms in the
304 region. Using the ArcHydrology toolbox and a MATLAB script program (StreamProfiler;
305 Whipple et al., 2007) to extract the river longitudinal profile and watershed catchment
306 area from SRTM data, the river slope can be calculated (Kirby and Whipple, 2012;
307 Zahra et al., 2017). The river channel morphology can be assessed by SA regression
308 to obtain concavity and steepness. The presence or absence of knickpoints can be
309 determined, shaping the subsequent analysis of knickpoint distribution or the shape of
310 the longitudinal profile (Figs. 3 and 4).

311

312 **4 Results**

313 Using ArcGIS 10.2, twenty-four river long-profiles from the Qianghe Graben were
314 extracted from the SRTM DEM. All tributaries are symmetrically distributed on both
315 sides of the main channel of the Qianhe and Jinlinghe Rivers. Twenty-three of them
316 cross TGF and QMF (Fig. 5). The longitudinal profile form and SA plots reveal
317 information regarding the underlying controls on river formation and elevation (Berlin
318 and Anderson, 2007; Harkins et al., 2007; Whittaker et al., 2007; Stokes et al., 2008;
319 Kirby and Whipple, 2012; Boulton et al., 2014; Giletycz et al., 2015), and record the
320 geomorphic constraints on uplift history (Olivetti et al., 2012; Rossi et al., 2017;
321 Robustelli, 2019). Therefore, the presence or absence of knickpoints was firstly
322 identified, allowing the subsequent analysis to be undertaken appropriately on the river
323 long profiles (Fig. 5). Sixteen rivers had knickpoints, of which eight rivers have two

324 knickpoints and eight rivers have one knickpoint. Eight rivers are found to be without
325 knickpoints. For comparative analysis, rivers to the northeast and southwest of River
326 11 are divided into two separate groups representing the two margins of the Qianhe
327 Graben.

328

329 The length of the rivers with knickpoints ranges from 54.6 - 160.1 km (Table 1), with
330 the longest river (R11) occurring in the center of Qianhe Graben and the shortest river
331 (R24) on the southern margin of the Qianhe Graben. The total drainage area of these
332 catchments varies between 3.3 and 194.9 km². As for the rivers without knickpoints,
333 these have an average length of 91.1 km (Table 2).

334

335 Fifteen rivers exhibit slope-break knickpoints (Figs. 5 and 6), while only River 2 has a
336 vertical-step knickpoint. These rivers have a moderate or high k_{sn} value, ranging from
337 11.0 to 115.0 m^{0.9} (Table 1 and Fig. 6). The average of k_{sn} values downstream of the
338 south and north rivers are 71.1 and 50.5 m^{0.9}, respectively, while the average k_{sn}
339 upstream are 41.0 and 27.1 m^{0.9}, respectively. Therefore, southern rivers have higher
340 k_{sn} values than northern rivers. River 10 has the highest k_{sn} values, where k_{sn} above
341 and below the knickpoint is 11.0 and 115.0 m^{0.9}, respectively (Table 1). The k_{sn} is
342 significantly higher below the knickpoint than above for rivers exhibiting slope-break
343 knickpoints, while the k_{sn} of the river with vertical-step knickpoint is similar above and
344 below the knickpoint (Fig. 6). For example, the k_{sn} above and below the vertical-step

345 knickpoint in River 2 is 16.8 and 34.8 $\text{m}^{0.9}$, respectively. While the rivers without
346 knickpoints only have one k_{sn} value, ranging from 30.1 to 80.4 $\text{m}^{0.9}$ (Table 2).

347

348 To investigate the change of k_{sn} from above to below the knickpoints, the k_{sn} ratios of
349 knickpoints can be investigated (Fig. 7). There is no significant difference between k_{sn}
350 ratios of most knickpoints, ranging from 0.8 - 10.5. The average k_{sn} ratios of south and
351 north knickpoints are 2.7 and 2.0, respectively. The k_{sn} values for River 9 and River 10
352 exceed 7, may confirm that the high change of slope in the north section of this study
353 area.

354

355 To analyse the vertical distribution of knickpoints, two swath profiles (NN' and SS') with
356 a width of 20 km along the strike and paralleling the QMF and TGF are drawn to
357 compare relief against the knickpoint elevation (Fig. 8a and b). Northern knickpoints
358 range between 1000 - 1400 m in elevation, while southern knickpoints decrease in
359 height from 2300 m to 1100 m southwards. There is an obvious feature that the
360 knickpoints elevation is consistent with the relief (Fig. 8). The knickpoints at the
361 northwestern section of the Qianhe Graben have much higher elevation, while the
362 southeastern section are lower. For example, River 10 has the highest knickpoint at
363 2245 m and the highest relief of 1141 m. The knickpoint elevation against relief in south
364 and north profiles (NN' and SS') are plotted (Fig. 8c and d) and show a stronger linear
365 relationship for the knickpoints on the southern rivers ($R^2 = 0.58$), than for the northern
366 rivers ($R^2 = 0.33$).

367

368 When the horizontal distribution of knickpoints is considered, slope-break knickpoints
369 are present consistently upstream of faults. Whereas the vertical-step knickpoint in
370 River 2 is located on the trace of the GGF (Fig. 5). Additionally, we observe that the
371 upstream distance of knickpoints from faults is greater when the drainage area is
372 larger (Fig. 9), where $L \sim A^{0.64}$ with an R^2 of 0.6. For example, River 10 has a drainage
373 area of 57.3 km² and the upstream distance of the knickpoint from the fault is 13.8 km,
374 while River 24 has a drainage area of 19.0 km², but the knickpoint has only migrated
375 7.8 km. This relationship demonstrates that the distance from faults to knickpoints
376 scale with drainage area in these river systems and the knickpoints propagate
377 upstream as a surrogate of stream discharge, in agreement with previous studies
378 (Boulton et al., 2014; Whittaker and Walker, 2015; Castillo, 2017; Kent et al., 2017).

379

380 It is interesting to note that the vertical-step knickpoint of River 2 is located on the GGF,
381 and at the boundary between Cretaceous and Ordovician sandstone (Figs. 1c and 5).
382 As previously discussed, vertical-step knickpoints are not directly related to uplift
383 (Haviv et al., 2010; Kirby and Whipple, 2012) and the potential for knickpoint migration
384 upstream is limited (Harkins et al., 2007; Wang et al., 2015). To investigate the
385 significance of the vertical-step knickpoint, further tributaries around River 2 were
386 obtained (Fig. 10a).

387

388 Eight vertical-step knickpoints were located on the GGF (Fig. 10a), and the difference
389 of the k_{sn} above and below vertical-step knickpoints is minor (Fig. 10b), ranging from
390 26.7 to 49.9 $m^{0.9}$ (Table 3). Interestingly other rivers in Qianhe Graben, such as Rivers
391 3 to 7, also cross the GGF but do not have the vertical-step knickpoints (Fig. 5). River
392 2 traverses the change from Cretaceous to Ordovician sandstones and limestones
393 whereas further north Cretaceous sediments are juxtaposed against Neogene
394 sediments of similar rheology (Fig. 1c). Therefore, the lithological strength contrast
395 across the fault is likely the cause of the vertical-step knickpoints, giving a new insight
396 into the location of this fault.

397

398 Finally, information on the eight longitudinal profiles without knickpoints was obtained
399 using $\log(S)$ curve on SA plot to reveal the uplift rate of these rivers, and applying
400 linear, exponential, logarithmic and power functions to regress the best shape for the
401 long profile (Table 2). As shown in Table 2, $\log(S)$ curves on SA plot are convex in
402 River 4, 13 and 15, and the other are linear. The logarithmic function is the best fit to
403 this subset of rivers, where the coefficients of determination (R^2) are > 0.9 (Table 2).
404 The exponent and power function are close to the logarithmic function, and $R^2 > 0.79$.
405 By contrast, the linear function shows a slightly weaker fit to the data. As discussed in
406 the methodology (Fig. 4b), the shape of logarithmic function shows that in all eight
407 channels incision is high, and the upstream material is transported the downstream
408 accumulation zones.

409

410 In summary, the southern margin of the Qianhe Graben has higher relief, elevation,
411 slope, and k_{sn} , while the northern region exhibits lower values for all variables. In
412 addition, the slope-break knickpoints are consistent with being the upstream extent of
413 a transient wave of incision. The reasons for this are explored in the following sections.

414

415 **5 Discussion**

416 **5.1 Why are there knickpoints?**

417 Previous studies have shown that knickpoints can be explained as the result of
418 transient fluvial incision across a region (Wobus et al., 2006; Berlin and Anderson,
419 2007; Stokes et al., 2008; Kirby and Whipple, 2012; Boulton et al., 2014), where the
420 topographic evolution is related to the interplay between climate, basement lithology
421 and tectonic uplift (Duvall, 2004; Burbank and Anderson, 2011; Kirby and Whipple,
422 2012; Whittaker and Boulton, 2012; Allen et al., 2013; D'Arcy and Whittaker, 2014;
423 Pérez-Fodich et al., 2014; Martins et al., 2017). In the study area, the knickpoint
424 characteristics are consistent with being the upstream extent of a transient wave of
425 incision, but what caused the landscape perturbation? Here we explore mechanisms
426 for knickpoint development.

427

428 Firstly, taking the annual mean precipitation distribution map in 2017 as a sample (Fig.
429 5b), the annual precipitation varies between 959 and 474 mm but with no clear N-S,
430 or W-E trends. There are also no clear trends shown in the annual precipitation maps
431 of the past 20 years. Additionally, the climatic changes over a longer period were also

432 considered. Sediment dating data records and the spatial-temporal distribution of
433 vegetation in the Chinese Loess Plateau (Sun et al., 2015, 2017; Xin et al., 2008)
434 suggest that the Holocene climate was dry and cold between 6 and 3 Ka (Wang et al.,
435 2012; Bian et al., 2014). Furthermore, the spatial distribution maps of geomorphic
436 parameters (e.g., hypsometric integral (HI), Stream length-gradient index (SL))
437 previously used to analyse the relationship between active tectonics and rainfall show
438 no obvious features (Shi et al., 2018; Zhang et al., 2019). Therefore, the knickpoints
439 are unlikely the result precipitation trends, as there is no real variation in rainfall along
440 the Qianhe Graben.

441

442 Secondly, knickpoints can be traced along rivers and it is clear that the slope-break
443 knickpoints do not fall on mapped lithological boundaries (Fig. 1c). Interestingly
444 northern knickpoints occur in Cretaceous sandstones, while the southern knickpoints
445 are found across a range of lithologies from Cretaceous sandstones to Early Paleozoic
446 diorite (Fig. 1c and 5). Previous studies have discussed that lithological resistance will
447 not increase the k_{sn} below knickpoints (Snyder et al., 2000; Wobus et al., 2006),
448 suggesting that the presence of most slope-break knickpoints in this area is not caused
449 by the lithological variation.

450

451 Finally, is knickpoint formation the result of an increase in footwall uplift related to
452 active faulting? The evidence of slope-break knickpoints, high topographic relief and

453 gorge formation downstream of knickpoints and that topographic relief scales with
454 knickpoint elevation (Fig. 8) is all consistent with a fault control on knickpoint formation.

455

456 In summary, the presence of slope-break knickpoints and other field evidence suggest
457 that knickpoint formation in the study area is the result of transient fluvial response to
458 fault uplift during the late Cenozoic. Furthermore, the vertical-step knickpoints here
459 cannot be ignored in that the lithological strength contrast at fault is likely the cause of
460 these vertical-step knickpoints, giving a new insight into fault location.

461

462 **5.2 Landscape response to active faults**

463 Previous studies have demonstrated that fault initiation or fault linkage results in an
464 acceleration of uplift, increasing channel steepness as a result of river incision (Tucker
465 and Whipple, 2002; Harkins et al., 2007; Whittaker and Boulton, 2012; Whittaker and
466 Walker, 2015). The horizontal rate of subsequent knickpoint migration is proportion to
467 stream discharge and drainage area (Crosby and Whipple, 2006; Boulton et al., 2014;
468 Whittaker and Walker, 2015; Castillo, 2017), while the vertical rate of knickpoint
469 migration depends on the relative magnitude of fault perturbation or base-level fall
470 (Wobus et al., 2006; Whittaker and Boulton, 2012). Previous studies have also shown
471 that the k_{sn} has a significant positive correlation with rock uplift rate (Snyder et al.,
472 2000; Wobus et al., 2006). However, k_{sn} is not directly transformable into uplift rates
473 (Snyder et al., 2000; Kirby et al., 2003). Using these principals, we can extract more
474 detail on the active faulting of the Qianhe Graben.

475

476 Firstly, the vertical component of knickpoint migration was measured as the elevation
477 difference between knickpoints (excluding vertical-step knickpoints) and the likely
478 causative fault (Fig. 11a). The mean and maximum channel elevation difference of this
479 area are ~ 482 and 1136 m, respectively. There is a small decrease from north to south
480 in the elevation difference of the northern knickpoints (Fig. 11b), ranging from 600 -
481 100 m in height and showing more or less in a linear trend. Southern knickpoints also
482 show a similar trend decreasing from 1150 m in the north to 180 m in the south. The
483 lowest knickpoint height occurs on River 5 at 159 m, which is slightly lower than
484 knickpoints in rivers on either side. Interestingly, this knickpoint is located at the step-
485 over between two segments of TGF (Fig. 5a).

486

487 Previous studies have discussed that a fault linkage increases fault uplift rates and
488 forms knickpoints in channels upstream of the linked area as a result of slip
489 acceleration owing to under-displacement of the fault in the linkage zone (Boulton and
490 Whittaker, 2009; Whittaker and Walker, 2015; Kent et al., 2017). In previous examples
491 (i.e., Boulton and Whittaker, 2009; Kent et al., 2017) the knickpoint height along the
492 strike of the fault clearly follows the overall displacement profile on the fault with a
493 number of rivers/knickpoints defining each linked segment. This is not the case for
494 rivers crossing the northern boundary fault of the Qianhe Graben with knickpoint height
495 generally decreasing to the southeast. Nor is there a clear pattern for the rivers
496 crossing the southwestern margin of the graben, although there is a height minima

497 corresponding to the relay ramp along the TGF but knickpoint elevations are high at
498 either end of the fault array. This pattern of knickpoints indicates that the trend along
499 the southwestern fault is either decreasing to the southeast, or more typical of fault
500 segments but the full length of the faults is longer than previously mapped.

501

502 Here we also note that two knickpoints are present on eight of the rivers, where one
503 knickpoint is high in the channel with an upstream catchment area between 1×10^7
504 m^2 and $1 \times 10^8 \text{m}^2$ (Fig. 5). Crosby and Whipple (2006) demonstrated that knickpoints
505 migrate upstream until channel incision at low drainage areas prevents efficient
506 incision and results in the knickpoint location at a threshold drainage area, which in
507 the case of the Waipaoa River (New Zealand) is between $1 \times 10^5 \text{m}^2$ and $1 \times 10^6 \text{m}^2$.
508 Therefore, our observations suggest that is unlikely that the upper knickpoints are
509 pinned at the threshold drainage area as the drainage areas are at least an order of
510 magnitude greater than recorded by Crosby and Whipple (2006), suggesting that the
511 upper knickpoints are still migrating through the landscape.

512

513 As both fault initiation and fault linkage will increase channel steepness and incision
514 causing knickpoint formation and propagation through the river system, it is likely that
515 both signals are being preserved in the landscape of the Qianhe Graben (Tucker and
516 Whipple, 2002; Whittaker and Boulton, 2012; Whittaker and Walker, 2015). Fault
517 initiation occurs prior to fault linkage and therefore, the first incisional wave is marked
518 by the higher knickpoint, while the lower knickpoints may be the result of later fault

519 linkage. Previous studies have shown that the fault segments may evolve without
520 obvious surface connection (soft linkage) or link by breaching the relay zone (hard
521 linkage) (Kim and Sanderson, 2005). There are no relay ramps on north-eastern side
522 of the graben in this study area, although two knickpoints in north-eastern rivers are
523 observed, while the south-western side has a relay ramps along TGF (Fig. 5).
524 Therefore, it is possible that the faults defined the north-eastern side of the graben
525 maybe hard-linked outside of the study area, while the south-western side could be
526 soft-linked across the known relay ramp.

527

528 Interestingly the south-western rivers also have overall higher k_{sn} than the north, which
529 along with higher elevation knickpoints, indicates that the south-western margin is
530 experiencing higher uplift rates. This interpretation is supported by other lines of
531 evidence. Firstly, Song et al. (2001) used paleomagnetic measurements and
532 morphostratigraphy of red bed/clay sequences from pediments to determine that the
533 Liupan Mountain has been uplifting since about 3.8 Ma. Secondly, Chen et al. (2018b)
534 measured the height of highest river terrace (T1 - T5) in the northern of Qianhe Graben,
535 ranging from 8 - 10 m, 20 - 30 m, 60 - 80 m, 130 - 160 m, and 220 - 260 m, suggesting
536 that there is regional uplift with rate of 0.5 - 1.5 mm/yr (Zhang et al., 2019). These
537 results support our observations and suggest that the north-eastern margin of the
538 Qianhe Graben is experiencing lower rates of uplift than the south-western margin.

539

540 Additionally, in terms of the eight longitudinal profiles without knickpoints, although
541 these rivers are not analyzed in a same way, they are still responding to the regional
542 uplift rate. For example, River 4 does not exhibit knickpoints on the longitudinal profiles
543 but shows a convex $\log(S)$ form on SA plot (Fig. 6), suggesting that the uplift rate $>$
544 erosion rate in this location. On the opposite margin, the River 17 shows a linear $\log(S)$
545 form on SA plot, indicating that the uplift rate \approx erosion rate. Therefore, the south-
546 western rivers without knickpoints have likely higher uplift rates than north-eastern
547 rivers as the erosion rate is assumed to be similar in the absence of erosion data.
548 Similar to the rivers exhibiting knickpoints, the k_{sn} is higher for the south-western rivers
549 without knickpoints than north-eastern rivers (Table 2), suggesting that the uplift rate
550 is higher in south-western margin of Qianhe Graben. Although, these results do not
551 give absolute values of uplift rates, these data provide additional evidence into
552 patterns of rock uplift where the rivers without knickpoints are located.

553

554 *Landscape response time*

555 Previous studies have demonstrated that knickpoint retreat rates act as a pivotal part
556 of the landscape response time, and that the propagation rate depends on the uplift
557 rate of faults and strength of basement rocks in tectonically active settings (Boulton
558 and Whittaker, 2009; Jansen et al., 2011; Whittaker and Boulton, 2012; Allen et al.,
559 2013; Castillo et al., 2013, 2017; Castillo, 2017; Kent et al., 2017). Therefore,
560 investigating the migration of the knickpoints triggered by fault uplift is another way to
561 reveal the landscape response to active faulting.

562

563 As shown in Fig. 9, the function ($L \sim A^{0.64}$) demonstrates that the knickpoints follow a
564 common scaling across the study area suggesting that the knickpoints formed at
565 similar times across the graben. Furthermore, the basal loess beds ages can be used
566 to determine the age of river incision as the isochrones of loess sequences can be
567 accurately recognized (Zhang et al., 2019). Based on magnetostratigraphy, previous
568 studies have shown that fault initiation occurred before 1.2 - 1.4 Myr (Chen et al.,
569 2018b; Zhang et al., 2019). Therefore, using the upstream distance from faults to
570 knickpoints and 1.2 - 1.4 Myr as the time of knickpoint formation, the retreat rates of
571 knickpoints was estimated (Fig. 12; Tables 1 and 4). We recognise that there are a
572 number of uncertainties herein regarding the knickpoint formation mechanism, the
573 timing of a) fault initiation and b) fault linkage, and how the terraces ages relate to
574 these events; however, in the absence of other constraints, the 1.2 - 1.4 Myr age range
575 allows us to estimate knickpoint retreat rates for the highest knickpoint in each river
576 (Fig. 12). Furthermore, this timescale is similar to knickpoint ages quoted elsewhere
577 for extensional systems (i.e., Boulton and Whittaker, 2009; Kent et al., 2017).

578

579 The retreat rates of knickpoints in Qianhe Graben range from 0.3 to 27.3 mm/yr (Table
580 4), similar to the Gediz Graben (4.5 - 28.0 mm/yr) (Kent et al., 2017), and the Central
581 Apennines of Italy (1.4 - 10.7 mm/yr) (Whittaker et al., 2007). As some previous studies
582 show (Whittaker and Boulton, 2012; Castillo et al., 2017), the retreat rates of
583 knickpoints increase quickly with the total drainage area above faults. As shown in Fig.

584 12, southern rivers with knickpoints have higher retreat rates and larger drainage area
585 above knickpoints than in the northern. For example, River 9 has higher knickpoint
586 retreat rate (27.3 mm/yr at 1.2 Myr) and total drainage area (139.1 km²), while the
587 River 5 has the lowest retreat rate (4.0 mm/yr at 1.2 Myr) and total drainage area (66.3
588 km²). Furthermore, knickpoints retreat rates of TGF and QMF decrease from north to
589 south along the strike of fault array, consistent with knickpoint elevation and k_{sn} , further
590 supporting the interpretation that the fault uplift will increase to the northwest and
591 decrease with the loss of stream discharge to southeast. These results above indicate
592 that the higher uplift rates induced the knickpoints to migrate further in the north.

593

594 Finally, to compare with other knickpoints in different sites (e.g., Hayakawa and
595 Matsukura, 2003; Bishop et al., 2005; Whittaker et al., 2007; Loget and Van Den
596 Driessche, 2009; Whittaker and Boulton, 2012; Ye et al., 2013; Castillo, 2017; Kent et
597 al., 2017), selecting 1.4 Myr as the minimum age of the fault initiation in Qianhe Graben
598 and all the knickpoints (except for the lower knickpoints) retreat rates against drainage
599 area are shown in Fig. 13. Of these different sites, the knickpoint retreat rates related
600 to Messinian Salinity Crisis (MSC) in the Mediterranean Sea (Loget and Van Den
601 Driessche, 2009) are the fastest (0.25 - 20.00 m/yr), occurred over 0.1 - 1.0 Myr, which
602 induced by base-level fall as a result of sea-level fall. While the retreat rates of Puerto
603 Vallarta in west-central Mexico (Castillo, 2017) are the slowest (0.07 - 0.72 mm/yr),
604 and the age of the rock uplift is 12.5 Kyr, which was caused by base-level fall as a
605 result of faulting.

606

607 Interestingly, published data can be divided into two groups based upon the
608 mechanism of knickpoint formation, where the first group induced by base-level fall as
609 a result of faulting has the higher linear fit ($R^2 = 0.80$), while linear fit of the second
610 group caused by eustatic sea-level fall is 0.62 (Fig. 13). These robust fits indicate that
611 the fault controlled knickpoints generally have slower retreat rates, than when
612 triggered by sea-level fall, and that fault slip rate likely strongly controls the speed of
613 knickpoint migration (c.f., Boulton and Whittaker, 2009).

614

615 When base-level fall as a result of sea-level fall is considered, the knickpoint retreat
616 rate does not seem to be related to the age of sea-level fall events. By contrast, the
617 retreat rates caused base-level fall as a result of faulting seem to be negatively related
618 to the time of faulting events, indicating that the older faulting events have lower
619 knickpoint retreat rates. Older faulting events having lower retreat rates can be
620 explained as a result of the drainage area decreasing as knickpoints migrate upstream
621 resulting in a loss of erosional efficiency and slowing down knickpoint migration
622 (Crosby and Whipple, 2006; Castillo, 2017).

623

624 However, it is not clear why this is also not true of sea-level fall knickpoints or why the
625 scaling relationship is different depending on the knickpoint trigger mechanism. Ye et
626 al., (2013) suggests that the knickpoint retreat rate on Tahiti may be independent of
627 drainage area as a result of the generally small size of the catchments studied. Yet,

628 this is not the case for knickpoints studied by Loget and Van Den Driessche (2009)
629 who show the drainage area dependency on knickpoints formed during the MSC.
630 Therefore, the difference in scaling is unlikely the result of drainage area differences.
631 However, it is notable that most sea-level fall knickpoints are described as steep
632 waterfalls that migrate because of plunge-pool erosion (i.e., Ye et al., 2013) as
633 opposed to stream-power dependent erosion along a steep bedrock river. Therefore,
634 we hypothesise that different mechanisms of erosion account for the difference in
635 scaling observed.

636

637 **5.3 Fault linkage causing knickpoints**

638 As shown previously, we hypothesize that the two segments of TGF faults are currently
639 linked (Fig. 5a and 14a). However, relay breaching faults are not observed leading to
640 some uncertainty in the current fault geometry. Fault linkage and growth are important
641 processes in basin-bounding normal fault systems (Peacock, 2002; Kairanov et al.,
642 2019) where normal fault segments are composed of overlapping segments (Childs et
643 al., 2009; Wang et al., 2018a). Previous studies have addressed that fault growth
644 occurs via increasing fault length and displacement (Walsh and Watterson, 1988;
645 Walsh et al., 2003), where the final fault length will be estimated by the fault's slip
646 history and will grow mainly by displacement accrual (Nicol et al., 2010; Jackson and
647 Rotevatn, 2013; Rotevatn et al., 2018). Additionally, the fault displacement-length
648 model (Wells and Coppersmith, 1994; Soliva and Benedicto, 2004; Kim and
649 Sanderson, 2005; Rotevatn et al., 2018; Wang et al., 2018a), allows individual faults

650 to have finite lengths and thus along-strike strain or displacement variations can be
651 predicted (Nicol et al., 2002; Fossen and Rotevatn, 2016). Therefore, these models of
652 fault scaling can be used to study the character of normal TGF growth and linkage.

653

654 Many researchers have proposed that faults have a constant d_{max}/L ratio for individual
655 fault arrays (Soliva and Benedicto, 2004; Kim and Sanderson, 2005; Schultz et al.,
656 2008; Soliva et al., 2008; Li et al., 2018; Torabi et al., 2019), where the d_{max} and L are
657 the maximum cumulative displacement on a fault and the maximum length of the fault,
658 respectively. The d_{max}/L ratio depends on the tectonic regime and the rate of fault
659 propagation (Peacock and Sanderson, 1996; Kim and Sanderson, 2005).

660

661 As shown in Fig. 14a, two stages are used to describe the patterns of TGF (southern
662 fault) before and after fault linkages. During stage 1, two initially isolated fault
663 segments of TGF are 40.1 and 48.3 km in length, respectively, and propagate towards
664 each other. The displacements of north and southern sections are calculated by the
665 ratio $d_{max}/L = 0.04$ (Kim et al., 2001), resulting in a displacement of 1.6 and 1.9 km,
666 respectively (Fig. 14b). At stage 2, the faults segments interact with each other and
667 may be linked by breaching the relay zone (Fig. 14a). After linkage, fault length will be
668 84.9 km (Fig. 14c). The displacement is estimated by the ratio $d_{max}/L = 0.025$ (Kim and
669 Sanderson, 2005), resulting in a predicted displacement of 2.1 km after fault linkage
670 (Fig. 14b). This event will cause slip rates to increase in the center of the fault as a

671 result of under displacement resulting in a second phase of knickpoint propagation to
672 take place.

673

674 This thought experiment is important because it can reveal how normal faults grow
675 and link in the basin, the frequency and magnitude of seismic hazard along the length
676 of a fault array (Cowie and Roberts, 2001; Soliva et al., 2008; Boulton and Whittaker,
677 2009; Nicol et al., 2010; Kent et al., 2017) and the long-term tectono-stratigraphic
678 development of graben (Gawthorpe and Leeder, 2000; Ge et al., 2018). The seismic
679 hazard of this loess-covered area is not well known. Therefore, it is possible to use the
680 fault displacement-length model and fault surface rupture length to predict the
681 magnitude of potential earthquakes before and after fault linkage. In an earthquake,
682 between one-half and one-third of the total fault length will rupture (Mark, 1977;
683 Kayabali and Akin, 2003). Following Wells and Coppersmith (1994), the magnitude
684 (M_w) can be expressed as follows:

685

$$M_w = 4.86 + 1.32 \log L \quad (8)$$

686 Where M_w is moment magnitude L is fault rupture length (in km).

687

688 For the northern TGF segment, rupture of one half to one third of the fault would be
689 13.4 and 20.1 km, while the ruptures of southern segments are 16.1 and 24.2 km,
690 respectively. Before linkage, this could result in earthquakes on the northern and
691 southern faults with predicted M_w of 6.3 - 6.6 and 6.5 - 6.7, respectively. After linkage,

692 the ruptures of one-third to one-half of the TGF are 28.3 and 42.5 km, potentially
693 resulting in an earthquake with predicted M_w of 6.8 - 7.0. As for the QMF in the northern
694 margin, the ruptures of one-third to one-half of the QMF are 21.0 and 31.5 km, and
695 there will be potential earthquake with predicted M_w of 6.6 - 6.8. These results are
696 similar to Cheng et al. (2014) discussed before ($M_w > 6.0$), and consistent with risk
697 map of this area (Fan et al., 2016). Therefore, even one-third of the fault segment will
698 produce a high magnitude earthquake and increase the risk of the seismic hazard after
699 fault linkage. This new finding not only shows the potential risk of seismic hazards
700 revealed by fault linkage event which previous studies never documented, but also
701 stresses that more attention should be paid to the relationship between earthquake
702 and fault length in this area.

703

704 **6 Conclusions**

705 To investigate the fault activity in the Qianhe Graben of Southwest margin of Ordos,
706 China, we used patterns of knickpoints in longitudinal profiles to analyse the transient
707 fluvial response to active faulting. Vertical-step knickpoints were identified along the
708 trace of the southern part of the GGF revealing new information on the location of this
709 little known structure. Whilst, slope-break knickpoints were identified across the region
710 and were interpreted as the response to the initiation of the main northern (QMF) and
711 southern graben (TGF) boundary faults at 1.2 - 1.4 Myr. These knickpoints migrate
712 upstream, and the effects of the new tectonic boundary conditions propagate
713 throughout the catchment. Calculated retreat rates of knickpoints in this area are in

714 the range 0.3 - 27.3 mm/yr, and consistent with other studies of fault-driven knickpoint
715 formation. Comparison with other previous studies suggests that knickpoints
716 recession induced by base-level fall as a result of faulting are relatively slower than
717 base-level fall as result of sea-level fall.

718

719 Finally, although further research is required to confirm that the southern TGF fault
720 segments are linked, a displacement-length model is used to study the evolution of
721 two TGF isolated segments, and predict the potential earthquake magnitude before
722 and after fault linkage, resulting in M_w of 6.3 - 6.7 and 6.8 - 7.0, respectively.
723 Demonstrating that the growth and linkage of TGF will increase the magnitude and
724 frequency of the earthquakes and other hazards along this structure. All of these
725 observations derived from geomorphic analysis are powerful tools for the geoscientist
726 as they not only quantify the transient landscape response to active faulting but also
727 provide a new insights into seismic hazards and tectono-stratigraphic development,
728 especially in areas difficult to access. Such insights can be critical for future
729 sustainable environmental development and management in areas vulnerable to
730 seismic and related hazards.

731

732 **Acknowledgements**

733 This work was financially supported by the 1:50, 000 geological mapping in the loess
734 covered region of the map sheets: Caobizhen (I48E008021), Liangting (I48E008022),
735 Zhaoxian (I48E008023), Qianyang (I48E009021), Fengxiang (I48E009022), &

736 Yaojiagou (I48E009023) in Shaanxi Province, China, under Grant [DD-20160060], and
737 the project of open fund for key laboratory of land and resources degenerate and
738 unused land remediation, under Grant [SXDJ2017-7].

739

740 **References**

741 Allen, G.H., Barnes, J.B., Pavelsky, T.M., Kirby, E., 2013. Lithologic and tectonic
742 controls on bedrock channel form at the northwest Himalayan front. *J. Geophys.*
743 *Res. Earth Surf.* 118, 1806–1825. <https://doi.org/10.1002/jgrf.20113>

744 Arrowsmith, J.R., Zielke, O., 2009. Tectonic geomorphology of the San Andreas Fault
745 zone from high resolution topography: An example from the Cholame segment.
746 *Geomorphology* 113, 70–81. <https://doi.org/10.1016/j.geomorph.2009.01.002>

747 Azañón, J.M., Galve, J.P., Pérez-Peña, J. V, Giaconia, F., Carvajal, R., Booth-Rea,
748 G., Jabaloy, A., Vázquez, M., Azor, A., Roldán, F.J., 2015. Relief and drainage
749 evolution during the exhumation of the Sierra Nevada (SE Spain): Is denudation
750 keeping pace with uplift? *Tectonophysics* 663, 19–32.
751 <https://doi.org/10.1016/j.tecto.2015.06.015>

752 Berlin, M.M., Anderson, R.S., 2007. Modeling of knickpoint retreat on the Roan
753 Plateau, western Colorado. *J. Geophys. Res.* 112.
754 <https://doi.org/10.1029/2006jf000553>

755 Bian, H., Pang, J., Huang, C., Zha, X., Gao, P., Wang, X., Li, X., Wang, L., 2014. A
756 comparative study of chemical weathering intensity and element transport
757 features of loess-palaeosol in the upper reaches of Hanjiang and Weihe river
758 valleys, China. *Geogr. Res.* 33, 654. <https://doi.org/10.11821/dlyj201404006>

759 Bishop, P., Hoey, T.B., Jansen, J.D., Artza, I.L., 2005. Knickpoint recession rate and
760 catchment area: the case of uplifted rivers in Eastern Scotland. *Earth Surf.*
761 *Process. Landforms* 30, 767–778. <https://doi.org/10.1002/esp.1191>

762 Boulton, S.J., Stokes, M., 2018. Which DEM is best for analyzing fluvial landscape
763 development in mountainous terrains? *Geomorphology* 310, 168–187.
764 <https://doi.org/10.1016/j.geomorph.2018.03.002>

765 Boulton, S.J., Stokes, M., Mather, A.E., 2014. Transient fluvial incision as an indicator
766 of active faulting and Plio-Quaternary uplift of the Moroccan High Atlas.
767 *Tectonophysics* 633, 16–33. <https://doi.org/10.1016/j.tecto.2014.06.032>

768 Boulton, S.J., Whittaker, A.C., 2009. Quantifying the slip rates, spatial distribution and
769 evolution of active normal faults from geomorphic analysis: Field examples from
770 an oblique-extensional graben, southern Turkey. *Geomorphology* 104, 299–316.
771 <https://doi.org/10.1016/j.geomorph.2008.09.007>

772 Burbank, D.W., Anderson, R.S., 2011. *Tectonic Geomorphology: Second Edition,*
773 *Tectonic Geomorphology: Second Edition.*
774 <https://doi.org/10.1002/9781444345063>

775 Castelltort, S., Goren, L., Willett, S.D., Champagnac, J.-D., Herman, F., Braun, J.,
776 2012. River drainage patterns in the New Zealand Alps primarily controlled by
777 plate tectonic strain. *Nat. Geosci.* 5, 744–748. <https://doi.org/10.1038/ngeo1582>

778 Castillo, M., 2017. Landscape evolution of the graben of Puerto Vallarta (west-central
779 Mexico) using the analysis of landforms and stream long profiles. *J. South Am.*
780 *Earth Sci.* 73, 10–21. <https://doi.org/10.1016/j.jsames.2016.11.002>

781 Castillo, M., Bishop, P., Jansen, J.D., 2013. Knickpoint retreat and transient bedrock
782 channel morphology triggered by base-level fall in small bedrock river catchments:
783 The case of the Isle of Jura, Scotland. *Geomorphology* 180–181, 1–9.
784 <https://doi.org/10.1016/j.geomorph.2012.08.023>

785 Castillo, M., Ferrari, L., Muñoz-Salinas, E., 2017. Knickpoint retreat and landscape
786 evolution of the Amatlán de Cañas half-graben (northern sector of Jalisco Block,
787 western Mexico). *J. South Am. Earth Sci.* 77, 108–122.
788 <https://doi.org/10.1016/j.jsames.2017.05.003>

789 Castillo, M., Muñoz-Salinas, E., Ferrari, L., 2014. Response of a landscape to
790 tectonics using channel steepness indices (ksn) and OSL: A case of study from

791 the Jalisco Block, Western Mexico. *Geomorphology* 221, 204–214.
792 <https://doi.org/10.1016/j.geomorph.2014.06.017>

793 Chen, J., Zhang, Z., Li, H., Survey, S.I. of G., 2004. The regional geological survey
794 reports of 1: 250 000 Baoji city. Shaanxi Institute of Geological Survey.

795 Chen, M., Hu, X., Wang, W., 2018a. The cause of high-altitude knickpoints on river
796 longitudinal profiles along the Zoulang Nan Shan. *Acta Geogr. Sin.* 73, 1702–
797 1713. <https://doi.org/10.11821/dlxb201809007>

798 Chen, S., Fan, S., Wang, X., Wang, R., Liu, Y., Yang, L., Ning, X., Li, R., Li, S., 2018b.
799 Neotectonic movement in the southern margin of the Ordos Block inferred from
800 the Qianhe River terraces near the north of the Qinghai-Tibet Plateau. *Geol. J.* 53,
801 274–281. <https://doi.org/10.1002/gj.3111>

802 Chen, Y.-C., Sung, Q., Chen, C.-N., 2006. Stream-power incision model in non-
803 steady-state mountain ranges: An empirical approach. *Chinese Sci. Bull.* 51,
804 2789–2794. <https://doi.org/10.1007/s11434-006-2194-x>

805 Chen, Y.-C., Sung, Q., Cheng, K.-Y., 2003. Along-strike variations of morphotectonic
806 features in the Western Foothills of Taiwan: tectonic implications based on
807 stream-gradient and hypsometric analysis. *Geomorphology* 56, 109–137.
808 [https://doi.org/10.1016/s0169-555x\(03\)00059-x](https://doi.org/10.1016/s0169-555x(03)00059-x)

809 Cheng, B., Cheng, S., Zhang, G., Zhao, D., 2014. Seismic structure of the Helan–
810 Liupan–Ordos western margin tectonic belt in North-Central China and its
811 geodynamic implications. *J. Asian Earth Sci.* 87, 141–156.
812 <https://doi.org/10.1016/j.jseaes.2014.01.006>

813 Cheng, Y., He, C., Rao, G., Yan, B., Lin, A., Hu, J., Yu, Y., Yao, Q., 2018.
814 Geomorphological and structural characterization of the southern Weihe Graben,
815 central China: Implications for fault segmentation. *Tectonophysics* 722, 11–24.
816 <https://doi.org/10.1016/j.tecto.2017.10.024>

817 Childs, C., Manzocchi, T., Walsh, J.J., Bonson, C.G., Nicol, A., Schöpfer, M.P.J., 2009.
818 A geometric model of fault zone and fault rock thickness variations. *J. Struct. Geol.*
819 31, 117–127. <https://doi.org/10.1016/j.jsg.2008.08.009>

- 820 Cowie, P.A., Roberts, G.P., 2001. Constraining slip rates and spacings for active
821 normal faults. *J. Struct. Geol.* 23, 1901–1915. [https://doi.org/10.1016/S0191-](https://doi.org/10.1016/S0191-8141(01)00036-0)
822 8141(01)00036-0
- 823 Crosby, B.T., Whipple, K.X., 2006. Knickpoint initiation and distribution within fluvial
824 networks: 236 waterfalls in the Waipaoa River, North Island, New Zealand.
825 *Geomorphology* 82, 16–38. <https://doi.org/10.1016/j.geomorph.2005.08.023>
- 826 Cyr, A.J., Granger, D.E., Olivetti, V., Molin, P., 2014. Distinguishing between tectonic
827 and lithologic controls on bedrock channel longitudinal profiles using cosmogenic
828 ¹⁰Be erosion rates and channel steepness index. *Geomorphology* 209, 27–38.
829 <https://doi.org/10.1016/j.geomorph.2013.12.010>
- 830 D’Arcy, M., Whittaker, A.C., 2014. Geomorphic constraints on landscape sensitivity to
831 climate in tectonically active areas. *Geomorphology* 204, 366–381.
832 <https://doi.org/10.1016/j.geomorph.2013.08.019>
- 833 Dong, S., Zhang, P., Zhang, H., Zheng, W., Chen, H., 2017. Drainage Responses to
834 the Activity of the Langshan Range-Front Fault and Tectonic Implications. *J. Earth*
835 *Sci.* 29, 193–209. <https://doi.org/10.1007/s12583-017-0902-8>
- 836 Duvall, A., 2004. Tectonic and lithologic controls on bedrock channel profiles and
837 processes in coastal California. *J. Geophys. Res.* 109.
838 <https://doi.org/10.1029/2003jf000086>
- 839 Faghih, A., Esmaeilzadeh Soudejani, A., Nourbakhsh, A., Rokni, S., 2015. Tectonic
840 geomorphology of High Zagros Ranges, SW Iran: an initiative towards seismic
841 hazard assessment. *Environ. Earth Sci.* 74, 3007–3017.
842 <https://doi.org/10.1007/s12665-015-4331-9>
- 843 Fan, J., Ma, J., Gan, W., 2003. Movement of Ordos block and alternation of activity
844 along its boundaries. *Sci. China Ser. D Earth Sci.* 46, 168–180.
845 <https://doi.org/10.1360/03dz0013>
- 846 Fan, S.-H., Chen, S.-E., Li, R., Li, S., 2018. Combined effects of the subductions of
847 the Pacific Plate and Indian Plate in Central China in the Cenozoic: Recorded
848 from the Wei River Basin. *Geol. J.* 53, 266–273. <https://doi.org/10.1002/gj.3098>

849 Fan, S., Li, R., Wang, R., 2016. the 1:50,000 geological mapping in the loess-covered
850 region with the map sheets: Caobizhen (I48E008 021), Liangting (I48E008022),
851 Zhaoxian(I48E008023), Qianyang (I48E009021), Feng xiang (I48E009022), and
852 Yaojiagou (I48E009023) in Shaanxi Province of China. Chang'an University,
853 China.

854 Farr, T.G., Rosen, P.A., Caro, E., Crippen, R., Duren, R., Hensley, S., Kobrick, M.,
855 Paller, M., Rodriguez, E., Roth, L., Seal, D., Shaffer, S., Shimada, J., Umland, J.,
856 Werner, M., Oskin, M., Burbank, D., Alsdorf, D., 2007. The Shuttle Radar
857 Topography Mission. *Rev. Geophys.* 45. <https://doi.org/10.1029/2005rg000183>

858 Flint, J.J., 1974. Stream gradient as a function of order, magnitude, and discharge.
859 *Water Resour. Res.* 10, 969–973. <https://doi.org/10.1029/WR010i005p00969>

860 Fossen, H., Rotevatn, A., 2016. Fault linkage and relay structures in extensional
861 settings—A review. *Earth-Science Rev.* 154, 14–28.
862 <https://doi.org/10.1016/j.earscirev.2015.11.014>

863 Gailleton, B., Mudd, S.M., Clubb, F.J., Peifer, D., Hurst, M.D., 2019. A segmentation
864 approach for the reproducible extraction and quantification of knickpoints from
865 river long profiles. *Earth Surf. Dyn.* 7, 211–230. [https://doi.org/10.5194/esurf-7-](https://doi.org/10.5194/esurf-7-211-2019)
866 [211-2019](https://doi.org/10.5194/esurf-7-211-2019)

867 Gawthorpe, R.L., Leeder, M.R., 2000. Tectono-sedimentary evolution of active
868 extensional basins. *Basin Res.* 12, 195–218. [https://doi.org/10.1111/j.1365-](https://doi.org/10.1111/j.1365-2117.2000.00121.x)
869 [2117.2000.00121.x](https://doi.org/10.1111/j.1365-2117.2000.00121.x)

870 Ge, Z., Nemeč, W., Gawthorpe, R.L., Rotevatn, A., Hansen, E.W.M., 2018. Response
871 of unconfined turbidity current to relay-ramp topography: insights from process-
872 based numerical modelling. *Basin Res.* 30, 321–343.
873 <https://doi.org/10.1111/bre.12255>

874 Giletycz, S., Loget, N., Chang, C.P., Mouthereau, F., 2015. Transient fluvial landscape
875 and preservation of low-relief terrains in an emerging orogen: Example from
876 Hengchun Peninsula, Taiwan. *Geomorphology* 231, 169–181.
877 <https://doi.org/10.1016/j.geomorph.2014.11.026>

878 Guo, X., Gao, R., Li, S., Xu, X., Huang, X., Wang, H., Li, W., Zhao, S., Li, X., 2016.
879 Lithospheric architecture and deformation of NE Tibet: New insights on the
880 interplay of regional tectonic processes. *Earth Planet. Sci. Lett.* 449, 89–95.
881 <https://doi.org/10.1016/j.epsl.2016.05.045>

882 Hack, J.T., 1973. Stream-profile analysis and stream-gradient index. *J. Res. U.S. Geol.*
883 *Surv.* 1, 421–429.

884 Hack, J.T., 1957. *Studies of Longitudinal Stream Profiles in Virginia and Maryland.*
885 *Geol. Surv. Prof. Pap.*

886 Han, L., Liu, Z., Ning, Y., Zhao, Z., 2018. Extraction and analysis of geological
887 lineaments combining a DEM and remote sensing images from the northern Baoji
888 loess area. *Adv. Sp. Res.* 62, 2480–2493.
889 <https://doi.org/10.1016/j.asr.2018.07.030>

890 Hancock, G.R., Martinez, C., Evans, K.G., Moliere, D.R., 2006. A comparison of SRTM
891 and high-resolution digital elevation models and their use in catchment
892 geomorphology and hydrology: Australian examples. *Earth Surf. Process.*
893 *Landforms* 31, 1394–1412. <https://doi.org/10.1002/esp.1335>

894 Harkins, N., Kirby, E., Heimsath, A., Robinson, R., Reiser, U., 2007. Transient fluvial
895 incision in the headwaters of the Yellow River, northeastern Tibet, China. *J.*
896 *Geophys. Res.* 112. <https://doi.org/10.1029/2006jf000570>

897 Haviv, I., Enzel, Y., Whipple, K.X., Zilberman, E., Matmon, A., Stone, J., Fifield, K.L.,
898 2010. Evolution of vertical knickpoints (waterfalls) with resistant caprock: Insights
899 from numerical modeling. *J. Geophys. Res.* 115.
900 <https://doi.org/10.1029/2008jf001187>

901 Hayakawa, Y., Matsukura, Y., 2003. Recession rates of waterfalls in Boso Peninsula,
902 Japan, and a predictive equation. *Earth Surf. Process. Landforms* 28, 675–684.
903 <https://doi.org/10.1002/esp.519>

904 Hergarten, S., Robl, J., Stüwe, K., 2016. Tectonic geomorphology at small catchment
905 sizes – extensions of the stream-power approach and the
906 χ method. *Earth Surf. Dyn.* 4, 1–9.
907 <https://doi.org/10.5194/esurf-4-1-2016>

908 Hou, J.-J., Han, M.-K., Chai, B.-L., Han, H.-Y., 1998. Geomorphological observations
909 of active faults in the epicentral region of the Huaxian large earthquake in 1556 in
910 Shaanxi Province, China. *J. Struct. Geol.* 20, 549–557.
911 [https://doi.org/10.1016/S0191-8141\(97\)00112-0](https://doi.org/10.1016/S0191-8141(97)00112-0)

912 Howard, A.D., Dietrich, W.E., Seidl, M.A., 1994. Modeling Fluvial Erosion on Regional
913 to Continental Scales. *J. Geophys. Res. Solid Earth* 99, 13971–13986.
914 <https://doi.org/10.1029/94jb00744>

915 Howard, A.D., Kerby, G., 1983. Channel Changes in Badlands. *Geol. Soc. Am. Bull.*
916 94, 739–752. [https://doi.org/10.1130/0016-7606\(1983\)942.0.CO;2](https://doi.org/10.1130/0016-7606(1983)942.0.CO;2)

917 Jackson, C.A.L., Rotevatn, A., 2013. 3D seismic analysis of the structure and evolution
918 of a salt-influenced normal fault zone: A test of competing fault growth models. *J.*
919 *Struct. Geol.* 54, 215–234. <https://doi.org/10.1016/j.jsg.2013.06.012>

920 Jansen, J.D., Fabel, D., Bishop, P., Xu, S., Schnabel, C., Codilean, A.T., 2011. Does
921 decreasing paraglacial sediment supply slow knickpoint retreat? *Geology* 39,
922 543–546. <https://doi.org/10.1130/G32018.1>

923 Jiang, W., Han, Z., Zhang, J., Jiao, Q., 2016. Stream profile analysis, tectonic
924 geomorphology and neotectonic activity of the Damxung-Yangbajain rift in the
925 south Tibetan Plateau. *Earth Surf. Process. Landforms* 41, 1312–1326.
926 <https://doi.org/10.1002/esp.3899>

927 Kairanov, B., Marín, D., Escalona, A., Cardozo, N., 2019. Growth and linkage of a
928 basin-bounding fault system: Insights from the Early Cretaceous evolution of the
929 northern Polhem Subplatform, SW Barents Sea. *J. Struct. Geol.*
930 <https://doi.org/10.1016/j.jsg.2019.04.014>

931 Kale, V.S., Sengupta, S., Achyuthan, H., Jaiswal, M.K., 2014. Tectonic controls upon
932 Kaveri River drainage, cratonic Peninsular India: Inferences from longitudinal
933 profiles, morphotectonic indices, hanging valleys and fluvial records.
934 *Geomorphology* 227, 153–165. <https://doi.org/10.1016/j.geomorph.2013.07.027>

935 Kayabali, K., Akin, M., 2003. Seismic hazard map of Turkey using the deterministic
936 approach. *Eng. Geol.* 69, 127–137. [https://doi.org/10.1016/s0013-](https://doi.org/10.1016/s0013-7952(02)00272-7)
937 [7952\(02\)00272-7](https://doi.org/10.1016/s0013-7952(02)00272-7)

938 Kent, E., Boulton, S.J., Stewart, I.S., Whittaker, A.C., Alçiçek, M.C., 2016. Geomorphic
939 and geological constraints on the active normal faulting of the Gediz (Alaşehir)
940 Graben, Western Turkey. *J. Geol. Soc. London.* 173, 666–678.
941 <https://doi.org/10.1144/jgs2015-121>

942 Kent, E., Boulton, S.J., Whittaker, A.C., Stewart, I.S., Cihat Alçiçek, M., 2017. Normal
943 fault growth and linkage in the Gediz (Alaşehir) Graben, Western Turkey, revealed
944 by transient river long-profiles and slope-break knickpoints. *Earth Surf. Process.*
945 *Landforms* 42, 836–852. <https://doi.org/10.1002/esp.4049>

946 Kim, Y.-S., Andrews, J.R., Sanderson, D.J., 2001. Reactivated strike–slip faults:
947 examples from north Cornwall, UK. *Tectonophysics* 340, 173–194.
948 [https://doi.org/10.1016/S0040-1951\(01\)00146-9](https://doi.org/10.1016/S0040-1951(01)00146-9)

949 Kim, Y.-S., Sanderson, D.J., 2005. The relationship between displacement and length
950 of faults: a review. *Earth-Science Rev.* 68, 317–334.
951 <https://doi.org/10.1016/j.earscirev.2004.06.003>

952 Kirby, E., Ouimet, W., 2011. Tectonic geomorphology along the eastern margin of
953 Tibet: insights into the pattern and processes of active deformation adjacent to
954 the Sichuan Basin. *Geol. Soc. London, Spec. Publ.* 353, 165–188.
955 <https://doi.org/10.1144/sp353.9>

956 Kirby, E., Whipple, K., 2001. Quantifying differential rock-uplift rates via stream profile
957 analysis. *Geology* 29, 415–418. [https://doi.org/10.1130/0091-](https://doi.org/10.1130/0091-7613(2001)029<0415:qdrurv>2.0.co;2)
958 [7613\(2001\)029<0415:qdrurv>2.0.co;2](https://doi.org/10.1130/0091-7613(2001)029<0415:qdrurv>2.0.co;2)

959 Kirby, E., Whipple, K.X., 2012. Expression of active tectonics in erosional landscapes.
960 *J. Struct. Geol.* 44, 54–75. <https://doi.org/10.1016/j.jsg.2012.07.009>

961 Kirby, E., Whipple, K.X., Tang, W., Chen, Z., 2003. Distribution of active rock uplift
962 along the eastern margin of the Tibetan Plateau: Inferences from bedrock channel
963 longitudinal profiles. *J. Geophys. Res. Solid Earth* 108.
964 <https://doi.org/10.1029/2001jb000861>

965 Li, B., Ling, Z., Zhang, J., Chen, J., Ni, Y., Liu, C., 2018. Displacement-length ratios
966 and contractional strains of lunar wrinkle ridges in Mare Serenitatis and Mare

967 Tranquillitatis. J. Struct. Geol. 109, 27–37.
968 <https://doi.org/10.1016/j.jsg.2018.01.003>

969 Li, J., 1991. The environmental effects of the uplift of the Qinghai-Xizang Plateau. *Quat.*
970 *Sci. Rev.* 10, 479–483. [https://doi.org/10.1016/0277-3791\(91\)90041-R](https://doi.org/10.1016/0277-3791(91)90041-R)

971 Li, L., Xu, G., Hu, J., Yu, X., 2012. An analysis of relative active tectonics based on
972 DEM. *Geol. China* 39, 595-604 (in Chinese with English abstract).

973 Li, W., Dong, Y., Guo, A., Liu, X., Zhou, D., 2013. Chronology and tectonic significance
974 of Cenozoic faults in the Liupanshan Arcuate Tectonic Belt at the northeastern
975 margin of the Qinghai–Tibet Plateau. *J. Asian Earth Sci.* 73, 103–113.
976 <https://doi.org/10.1016/j.jseaes.2013.04.026>

977 Liang, M., Wang, Z., Zhou, S., Zong, K., Hu, Z., 2014. The provenance of Gansu Group
978 in Longxi region and implications for tectonics and paleoclimate. *Sci. China Earth*
979 *Sci.* 57, 1221–1228. <https://doi.org/10.1007/s11430-013-4787-y>

980 Lin, A., Rao, G., Yan, B., 2015. Flexural fold structures and active faults in the
981 northern–western Weihe Graben, central China. *J. Asian Earth Sci.* 114, 226–241.
982 <https://doi.org/10.1016/j.jseaes.2015.04.012>

983 Lin, X., Chen, H., Wyrwoll, K.-H., Batt, G.E., Liao, L., Xiao, J., 2011. The Uplift History
984 of the Haiyuan-Liupan Shan Region Northeast of the Present Tibetan Plateau:
985 Integrated Constraint from Stratigraphy and Thermochronology. *J. Geol.* 119,
986 372–393. <https://doi.org/10.1086/660190>

987 Loget, N., Van Den Driessche, J., 2009. Wave train model for knickpoint migration.
988 *Geomorphology* 106, 376–382. <https://doi.org/10.1016/j.geomorph.2008.10.017>

989 Mark, R.K., 1977. Application of linear statistical models of earthquake magnitude
990 versus fault length in estimating maximum expectable earthquakes. *Geology* 5,
991 464–466. [https://doi.org/10.1130/0091-7613\(1977\)5<464:aolsmo>2.0.co;2](https://doi.org/10.1130/0091-7613(1977)5<464:aolsmo>2.0.co;2)

992 Martins, A.A., Cabral, J., Cunha, P.P., Stokes, M., Borges, J., Caldeira, B., Martins,
993 A.C., 2017. Tectonic and lithological controls on fluvial landscape development in
994 central-eastern Portugal: Insights from long profile tributary stream analyses.
995 *Geomorphology* 276, 144–163. <https://doi.org/10.1016/j.geomorph.2016.10.012>

- 996 Matoš, B., Pérez-Peña, J.V., Tomljenović, B., 2016. Landscape response to recent
997 tectonic deformation in the SW Pannonian Basin: Evidence from DEM-based
998 morphometric analysis of the Bilogora Mt. area, NE Croatia. *Geomorphology* 263,
999 132–155. <https://doi.org/10.1016/j.geomorph.2016.03.020>
- 1000 Nexer, M., Authemayou, C., Schildgen, T., Hantoro, W.S., Molliex, S., Delcaillau, B.,
1001 Pedoja, K., Husson, L., Regard, V., 2015. Evaluation of morphometric proxies for
1002 uplift on sequences of coral reef terraces: A case study from Sumba Island
1003 (Indonesia). *Geomorphology* 241, 145–159.
1004 <https://doi.org/10.1016/j.geomorph.2015.03.036>
- 1005 Nicol, A., Gillespie, P.A., Childs, C., Walsh, J.J., 2002. Relay zones between
1006 mesoscopic thrust faults in layered sedimentary sequences. *J. Struct. Geol.* 24,
1007 709–727. [https://doi.org/10.1016/S0191-8141\(01\)00113-4](https://doi.org/10.1016/S0191-8141(01)00113-4)
- 1008 Nicol, A., Walsh, J.J., Villamor, P., Seebeck, H., Berryman, K.R., 2010. Normal fault
1009 interactions, paleoearthquakes and growth in an active rift. *J. Struct. Geol.* 32,
1010 1101–1113. <https://doi.org/10.1016/j.jsg.2010.06.018>
- 1011 Ohmori, H., 1991. Change in the Mathematical Function Type Describing the
1012 Longitudinal Profile of a River through an Evolutionary Process. *J. Geol.* 99, 97–
1013 110. <https://doi.org/10.1086/629476>
- 1014 Olivetti, V., Cyr, A.J., Molin, P., Faccenna, C., Granger, D.E., 2012. Uplift history of
1015 the Sila Massif, southern Italy, deciphered from cosmogenic¹⁰Be erosion rates
1016 and river longitudinal profile analysis. *Tectonics* 31, n/a-n/a.
1017 <https://doi.org/10.1029/2011tc003037>
- 1018 Owen, L.A., D. Richardson, N. Castree, M. F. Goodchild, A. Kobayashi, Marston, R.A.,
1019 2017. Tectonic Geomorphology, in: *International Encyclopedia of Geography*.
1020 <https://doi.org/10.1002/9781118786352.wbieg0606>
- 1021 Ozkaymak, Ç., Sözbilir, H., 2012. Tectonic geomorphology of the Spildağı High
1022 Ranges, western Anatolia. *Geomorphology* 173–174, 128–140.
1023 <https://doi.org/10.1016/j.geomorph.2012.06.003>

1024 Peacock, D.C.P., 2002. Propagation, interaction and linkage in normal fault systems.
1025 Earth-Science Rev. 58, 121–142. [https://doi.org/10.1016/S0012-8252\(01\)00085-](https://doi.org/10.1016/S0012-8252(01)00085-)
1026 X

1027 Peacock, D.C.P., Sanderson, D.J., 1996. Effects of propagation rate on displacement
1028 variations along faults. J. Struct. Geol. 18, 311–320.
1029 [https://doi.org/10.1016/S0191-8141\(96\)80052-6](https://doi.org/10.1016/S0191-8141(96)80052-6)

1030 Pérez-Fodich, A., Reich, M., Álvarez, F., Snyder, G.T., Schoenberg, R., Vargas, G.,
1031 Muramatsu, Y., Fehn, U., 2014. Climate change and tectonic uplift triggered the
1032 formation of the Atacama Desert's giant nitrate deposits. Geology 42, 251–254.
1033 <https://doi.org/10.1130/g34969.1>

1034 Rădoane, M., Rădoane, N., Dumitriu, D., 2003. Geomorphological evolution of
1035 longitudinal river profiles in the Carpathians. Geomorphology 50, 293–306.
1036 [https://doi.org/10.1016/s0169-555x\(02\)00194-0](https://doi.org/10.1016/s0169-555x(02)00194-0)

1037 Rao, G., Cheng, Y., Lin, A., Yan, B., 2017. Relationship between landslides and active
1038 normal faulting in the epicentral area of the AD 1556 M~8.5 Huaxian Earthquake,
1039 SE Weihe Graben (Central China). J. Earth Sci. 28, 545–554.
1040 <https://doi.org/10.1007/s12583-017-0900-z>

1041 Regalla, C., Kirby, E., Fisher, D., Bierman, P., 2013. Active forearc shortening in
1042 Tohoku, Japan: Constraints on fault geometry from erosion rates and fluvial
1043 longitudinal profiles. Geomorphology 195, 84–98.
1044 <https://doi.org/10.1016/j.geomorph.2013.04.029>

1045 Ren, Z., Cui, J., Ke, G., Tao, T., Cao, Z., 2015. Fission-track analysis of uplift times
1046 and processes of the Weibei Uplift in the Ordos Basin. Chinese Sci. Bull. 60, 1298
1047 (in Chinese with English abstract). <https://doi.org/10.1360/N972014-00617>

1048 Robustelli, G., 2019. Geomorphic constraints on uplift history in the Aspromonte
1049 Massif, southern Italy. Geomorphology 327, 319–337.
1050 <https://doi.org/10.1016/j.geomorph.2018.11.011>

1051 Rossi, M.W., Quigley, M.C., Fletcher, J.M., Whipple, K.X., Díaz-Torres, J.J., Seiler, C.,
1052 Fifield, L.K., Heimsath, A.M., 2017. Along-strike variation in catchment
1053 morphology and cosmogenic denudation rates reveal the pattern and history of

1054 footwall uplift, Main Gulf Escarpment, Baja California. *Geol. Soc. Am. Bull.* 129,
1055 837–854. <https://doi.org/10.1130/b31373.1>

1056 Rotevatn, A., Jackson, C.A.L., Tvedt, A.B.M., Bell, R.E., Blækkan, I., 2018. How do
1057 normal faults grow? *J. Struct. Geol.* <https://doi.org/10.1016/j.jsg.2018.08.005>

1058 Schanz, S.A., Montgomery, D.R., 2016. Lithologic controls on valley width and strath
1059 terrace formation. *Geomorphology* 258, 58–68.
1060 <https://doi.org/10.1016/j.geomorph.2016.01.015>

1061 Scherler, D., DiBiase, R.A., Fisher, G.B., Avouac, J.-P., 2017. Testing monsoonal
1062 controls on bedrock river incision in the Himalaya and Eastern Tibet with a
1063 stochastic-threshold stream power model. *J. Geophys. Res. Earth Surf.* 122,
1064 1389–1429. <https://doi.org/10.1002/2016JF004011>

1065 Schultz, R.A., Soliva, R., Fossen, H., Okubo, C.H., Reeves, D.M., 2008. Dependence
1066 of displacement–length scaling relations for fractures and deformation bands on
1067 the volumetric changes across them. *J. Struct. Geol.* 30, 1405–1411.
1068 <https://doi.org/10.1016/j.jsg.2008.08.001>

1069 Sembroni, A., Molin, P., 2018. Long-term drainage system evolution in the Wabe
1070 Shebele River basin (SE Ethiopia - SW Somalia). *Geomorphology* 320, 45–63.
1071 <https://doi.org/10.1016/j.geomorph.2018.08.001>

1072 Shi, W., 2011. The analysis of the development characteristic and activity about fault
1073 zone of Longxian-Baoji. Chang'an University, Xi'an.

1074 Snyder, N.P., Whipple, K.X., Tucker, G.E., Merritts, D.J., 2000. Landscape response
1075 to tectonic forcing: Digital elevation model analysis of stream profiles in the
1076 Mendocino triple junction region, northern California. *Geol. Soc. Am. Bull.* 112,
1077 1250–1263. [https://doi.org/10.1130/0016-
1078 7606\(2000\)112<1250:LRTTFD>2.0.CO;2](https://doi.org/10.1130/0016-7606(2000)112<1250:LRTTFD>2.0.CO;2)

1079 Soliva, R., Benedicto, A., 2004. A linkage criterion for segmented normal faults. *J.*
1080 *Struct. Geol.* 26, 2251–2267. <https://doi.org/10.1016/j.jsg.2004.06.008>

1081 Soliva, R., Benedicto, A., Schultz, R.A., Maerten, L., Micarelli, L., 2008. Displacement
1082 and interaction of normal fault segments branched at depth: Implications for fault

1083 growth and potential earthquake rupture size. *J. Struct. Geol.* 30, 1288–1299.
1084 <https://doi.org/10.1016/j.jsg.2008.07.005>

1085 Song, Y., Fang, X., Li, J., An, Z., Miao, X., 2001. The Late Cenozoic uplift of the Liupan
1086 Shan, China. *Sci. China Ser. D Earth Sci.* 44, 176–184.
1087 <https://doi.org/10.1007/BF02911985>

1088 Stokes, M., Mather, A.E., Belfoul, A., Farik, F., 2008. Active and passive tectonic
1089 controls for transverse drainage and river gorge development in a collisional
1090 mountain belt (Dades Gorges, High Atlas Mountains, Morocco). *Geomorphology*
1091 102, 2–20. <https://doi.org/10.1016/j.geomorph.2007.06.015>

1092 Sun, A., Guo, Z., Wu, H., Li, Q., Yu, Y., Luo, Y., Jiang, W., Li, X., 2017. Reconstruction
1093 of the vegetation distribution of different topographic units of the Chinese Loess
1094 Plateau during the Holocene. *Quat. Sci. Rev.*
1095 <https://doi.org/10.1016/j.quascirev.2017.08.006>

1096 Sun, J., 2005. Long-term fluvial archives in the Fen Wei Graben, central China, and
1097 their bearing on the tectonic history of the India?Asia collision system during the
1098 Quaternary. *Quat. Sci. Rev.* 24, 1279–1286.
1099 <https://doi.org/10.1016/j.quascirev.2004.08.018>

1100 Sun, W., Song, X., Mu, X., Gao, P., Wang, F., Zhao, G., 2015. Spatiotemporal
1101 vegetation cover variations associated with climate change and ecological
1102 restoration in the Loess Plateau. *Agric. For. Meteorol.*
1103 <https://doi.org/10.1016/j.agrformet.2015.05.002>

1104 Tepe, Ç., Sözbilir, H., 2017. Tectonic geomorphology of the Kemalpaşa Basin and
1105 surrounding horsts, southwestern part of the Gediz Graben, Western Anatolia.
1106 *Geodin. Acta* 29, 70–90. <https://doi.org/10.1080/09853111.2017.1317191>

1107 Topal, S., Keller, E., Bufe, A., Koçyiğit, A., 2016. Tectonic geomorphology of a large
1108 normal fault: Akşehir fault, SW Turkey. *Geomorphology* 259, 55–69.
1109 <https://doi.org/10.1016/j.geomorph.2016.01.014>

1110 Torabi, A., Alaei, B., Libak, A., 2019. Normal fault 3D geometry and displacement
1111 revisited: Insights from faults in the Norwegian Barents Sea. *Mar. Pet. Geol.* 99,
1112 135–155. <https://doi.org/10.1016/j.marpetgeo.2018.09.032>

- 1113 Tucker, G.E., Whipple, K.X., 2002. Topographic outcomes predicted by stream
1114 erosion models: Sensitivity analysis and intermodel comparison. *J. Geophys. Res.*
1115 *Solid Earth* 107, ETG 1-1-ETG 1-16. <https://doi.org/10.1029/2001jb000162>
- 1116 Walsh, J.J., Bailey, W.R., Childs, C., Nicol, A., Bonson, C.G., 2003. Formation of
1117 segmented normal faults: a 3-D perspective. *J. Struct. Geol.* 25, 1251–1262.
1118 [https://doi.org/10.1016/S0191-8141\(02\)00161-X](https://doi.org/10.1016/S0191-8141(02)00161-X)
- 1119 Walsh, J.J., Watterson, J., 1988. Analysis of the relationship between displacements
1120 and dimensions of faults. *J. Struct. Geol.* 10, 239–247.
1121 [https://doi.org/10.1016/0191-8141\(88\)90057-0](https://doi.org/10.1016/0191-8141(88)90057-0)
- 1122 Wang, H., Huang, C., Zhou, Y., Pang, J., Zha, X., Gu, H., Zhou, L., 2012. OSL dating
1123 of the Holocene paleoflood events on the Qianhe River in the Guanzhong Basin,
1124 China. *Sci. Sin. Terrae* 42, 390–401. <https://doi.org/10.1360/zd-2012-42-3-390>
- 1125 Wang, H.B., Zhou, B., Wu, S.R., Shi, J.S., Li, B., 2011. Characteristic analysis of large-
1126 scale loess landslides: a case study in Baoji City of Loess Plateau of Northwest
1127 China. *Hazards Earth Syst. Sci* 11, 1829–1837. <https://doi.org/10.5194/nhess-11-1829-2011>
- 1129 Wang, H.X., Fu, X.F., Liu, S.R., Chu, R., Liu, B., Shi, P.P., 2018. Quantitative
1130 discrimination of normal fault segment growth and its geological significance:
1131 example from the Tanan Depression, Tamtsag Basin, Mongolia. *Aust. J. Earth*
1132 *Sci.* 65, 711–725. <https://doi.org/10.1080/08120099.2018.1462850>
- 1133 Wang, N., Han, Z., Li, X., Chen, G., Wang, X., Lu, H., 2015. Tectonic uplift of Mt.
1134 Lushan indicated by the steepness indices of the river longitudinal profiles. *Acta*
1135 *Gepgraphica Sin.* 70, 1516–1525. <https://doi.org/10.11821/dlxb201509013>
- 1136 Wang, S., Jiang, F., Zhang, S., Liu, L., Zhu, L., 2017. Present Vertical Deformation
1137 and Tectonic Activity in Liupanshan and Its Adjacent Areas. *J. Geod. Geodyn.* 37,
1138 16–21. <https://doi.org/10.14075/j.jgg.2017.01.004>
- 1139 Wang, Y., Zheng, D., Pang, J., Zhang, H., Wang, W., Yu, J., Zhang, Z., Zheng, W.,
1140 Zhang, P., Li, Y., 2018. Using slope-area and apatite fission track analysis to
1141 decipher the rock uplift pattern of the Yumu Shan: New insights into the growth of

1142 the NE Tibetan Plateau. *Geomorphology* 308, 118–128.
1143 <https://doi.org/10.1016/j.geomorph.2018.02.006>

1144 Wells, D.L., Coppersmith, K.J., 1994. New empirical relationships among magnitude,
1145 rupture length, rupture width, rupture area, and surface displacement. *Bull.*
1146 *Seismol. Soc. Am.* 84, 974–1002.

1147 Whipple, K., Meade, B., 2006. Orogen response to changes in climatic and tectonic
1148 forcing. *Earth Planet. Sci. Lett.* 243, 218–228.
1149 <https://doi.org/10.1016/j.epsl.2005.12.022>

1150 Whipple, K., Wobus, C., Crosby, B., Kirby, E., Sheehan, D., 2007. New Tools for
1151 Quantitative Geomorphology: Extraction and Interpretation of Stream Profiles
1152 from Digital Topographic Data, in: *GSA Annual Meeting. NSF Geomorphology*
1153 *and Land Use Dynamics*, Boulder, CO.

1154 Whipple, K.X., 2009. The influence of climate on the tectonic evolution of mountain
1155 belts. *Nat. Geosci.* 2, 97–104. <https://doi.org/10.1038/ngeo413>

1156 Whipple, K.X., 2004. Bedrock rivers and the geomorphology of active orogens. *Annu.*
1157 *Rev. Earth Planet. Sci.* 32, 151.
1158 <https://doi.org/10.1146/annurev.earth.32.101802.120356>

1159 Whipple, K.X., 2002. Implications of sediment-flux-dependent river incision models for
1160 landscape evolution. *J. Geophys. Res.* 107.
1161 <https://doi.org/10.1029/2000jb000044>

1162 Whipple, K.X., DiBiase, R.A., Crosby, B.T., 2013. 9.28 Bedrock Rivers. *Treatise*
1163 *Geomorphol.* 550–573. <https://doi.org/10.1016/B978-0-12-374739-6.00254-2>

1164 Whipple, K.X., Tucker, G.E., 1999. Dynamics of the stream-power river incision model:
1165 Implications for height limits of mountain ranges, landscape response timescales,
1166 and research needs. *J. Geophys. Res. Solid Earth* 104, 17661–17674.
1167 <https://doi.org/doi:10.1029/1999JB900120>

1168 Whittaker, A.C., 2012. How do landscapes record tectonics and climate? *Lithosphere*
1169 4, 160–164. <https://doi.org/10.1130/rlf.l003.1>

- 1170 Whittaker, A.C., Attal, M., Cowie, P.A., Tucker, G.E., Roberts, G., 2008. Decoding
1171 temporal and spatial patterns of fault uplift using transient river long profiles.
1172 *Geomorphology* 100, 506–526. <https://doi.org/10.1016/j.geomorph.2008.01.018>
- 1173 Whittaker, A.C., Boulton, S.J., 2012. Tectonic and climatic controls on knickpoint
1174 retreat rates and landscape response times. *J. Geophys. Res. Earth Surf.* 117,
1175 F02024. <https://doi.org/10.1029/2011jf002157>
- 1176 Whittaker, A.C., Cowie, P.A., Attal, M., Tucker, G.E., Roberts, G.P., 2007. Contrasting
1177 transient and steady-state rivers crossing active normal faults: new field
1178 observations from the Central Apennines, Italy. *Basin Res.* 19, 529–556.
1179 <https://doi.org/10.1111/j.1365-2117.2007.00337.x>
- 1180 Whittaker, A.C., Walker, A.S., 2015. Geomorphic constraints on fault throw rates and
1181 linkage times: Examples from the Northern Gulf of Evia, Greece. *J. Geophys. Res.*
1182 *Earth Surf.* 120, 137–158. <https://doi.org/10.1002/2014jf003318>
- 1183 Wobus, C.W., Crosby, B.T., Whipple, K.X., 2006. Hanging valleys in fluvial systems:
1184 Controls on occurrence and implications for landscape evolution. *J. Geophys. Res.*
1185 111. <https://doi.org/10.1029/2005jf000406>
- 1186 Xin, Z., Xu, J., Zheng, W., 2008. Spatiotemporal variations of vegetation cover on the
1187 Chinese Loess Plateau (1981–2006): Impacts of climate changes and human
1188 activities. *Sci. China Ser. D Earth Sci.* 51, 67–78. [https://doi.org/10.1007/s11430-](https://doi.org/10.1007/s11430-007-0137-2)
1189 [007-0137-2](https://doi.org/10.1007/s11430-007-0137-2)
- 1190 Xue, L., Alemu, T., Gani, N.D., Abdelsalam, M.G., 2018. Spatial and temporal variation
1191 of tectonic uplift in the southeastern Ethiopian Plateau from morphotectonic
1192 analysis. *Geomorphology* 309, 98–111.
1193 <https://doi.org/10.1016/j.geomorph.2018.02.025>
- 1194 Yan, Z., Zhang, H., Fan, X., Du, X., 2015. Geomorphic indices of rivers and drainage
1195 in China's Longmen Shan Fault zone and their implications for regional tectonic
1196 activity. *Geodin. Acta* 27, 48–59. <https://doi.org/10.1080/09853111.2014.979533>
- 1197 Ye, F.-Y., Barriot, J.-P., Carretier, S., 2013. Initiation and recession of the fluvial
1198 knickpoints of the Island of Tahiti (French Polynesia). *Geomorphology* 186, 162–
1199 173. <https://doi.org/10.1016/j.geomorph.2012.12.031>

1200 Zahra, T., Paudel, U., Hayakawa, Y.S., Oguchi, T., 2017. Knickzone Extraction Tool
1201 (KET) – A new ArcGIS toolset for automatic extraction of knickzones from a DEM
1202 based on multi-scale stream gradients. *Open Geosci.* 9.
1203 <https://doi.org/10.1515/geo-2017-0006>

1204 Zhang, T., Fan, S., Chen, S., Li, S., Lu, Y., 2019. Geomorphic evolution and
1205 neotectonics of the Qianhe River Basin on the southwest margin of the Ordos
1206 Block, North China. *J. Asian Earth Sci.* 176, 184–195.
1207 <https://doi.org/10.1016/j.jseaes.2019.02.020>

1208

Figures and Tables

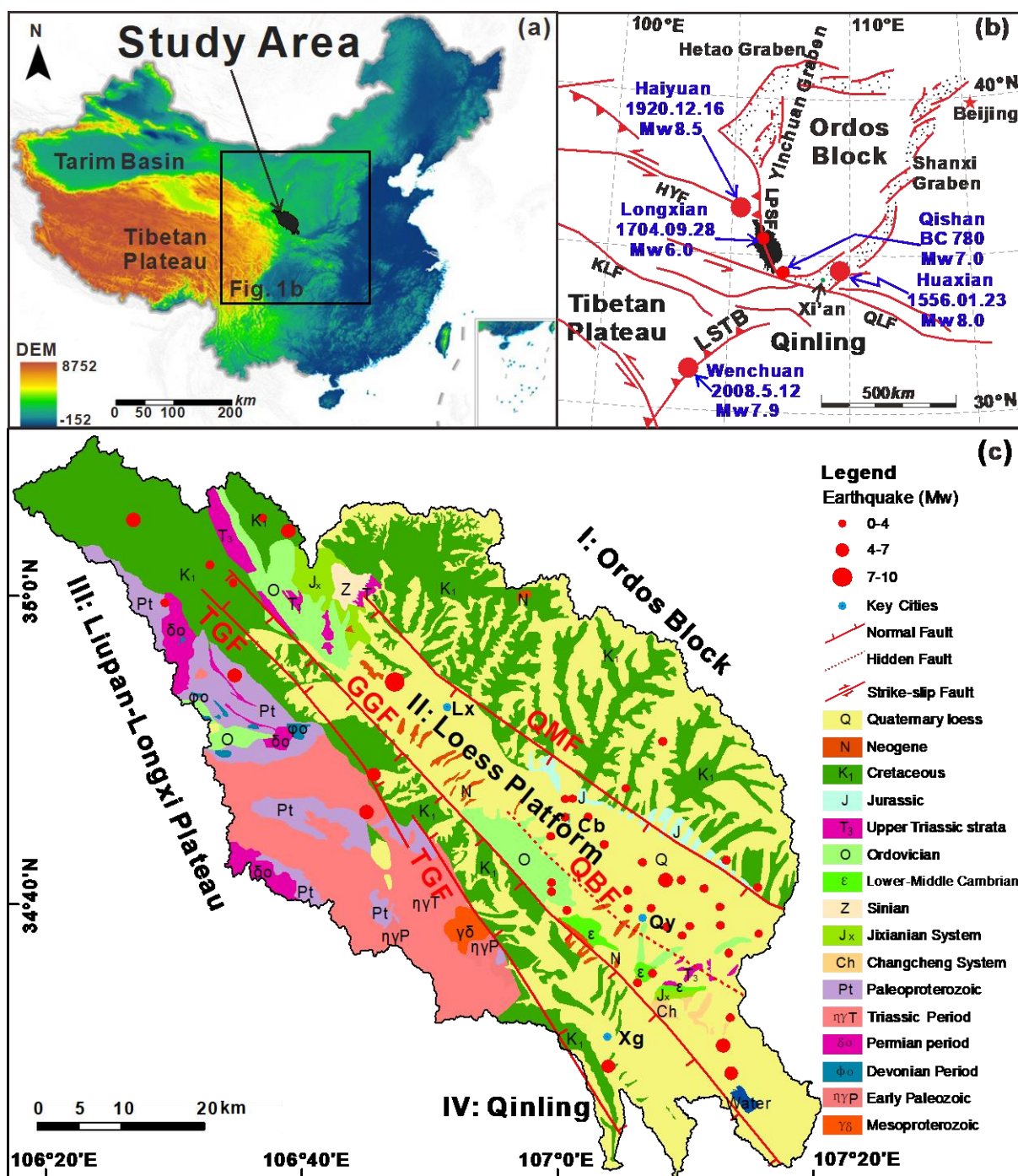


Fig. 1. Simplified regional geological map of Qianhe Basin. (a) map of China, data from <http://www.dsac.cn/>; (b) map of the regional geological background, adapted from (Rao et al., 2017; Cheng et al., 2018; Han et al., 2018), with earthquake data from (Cheng et al., 2014; Fan et al., 2016, 2018). The red lines are faults in central China: QLF: Qinling Fault; HYF: Haiyuan Fault; KLF: Kunlun Fault; LPSF: Liupanshan Fault; LSTB: Longmen Shan Thrust Belt; (c) The geological map modified from (Chen et al., 2004), showing the main lithologies and the significant regional faults. The four red NW faults are the target fault of this research, Qianhe Basin fault zone. QMF: Qishan-Mazhao Fault; QBF: Qianyang-Biaojiao Fault; GGF: Guguan-Guozhen Fault; TGF: Taoyuan-Guichuansi Fault. Key

cities: Lx, Longxian; Cb, Caobi; Qy, Qianyang; Xg, Xiangong. I: Uplift region of southwestern Ordos's margin; II: Differential descent area of Weihe Basin; III: Differential uplift region of Liupan-Longshan; IV: Qinling uplift area.

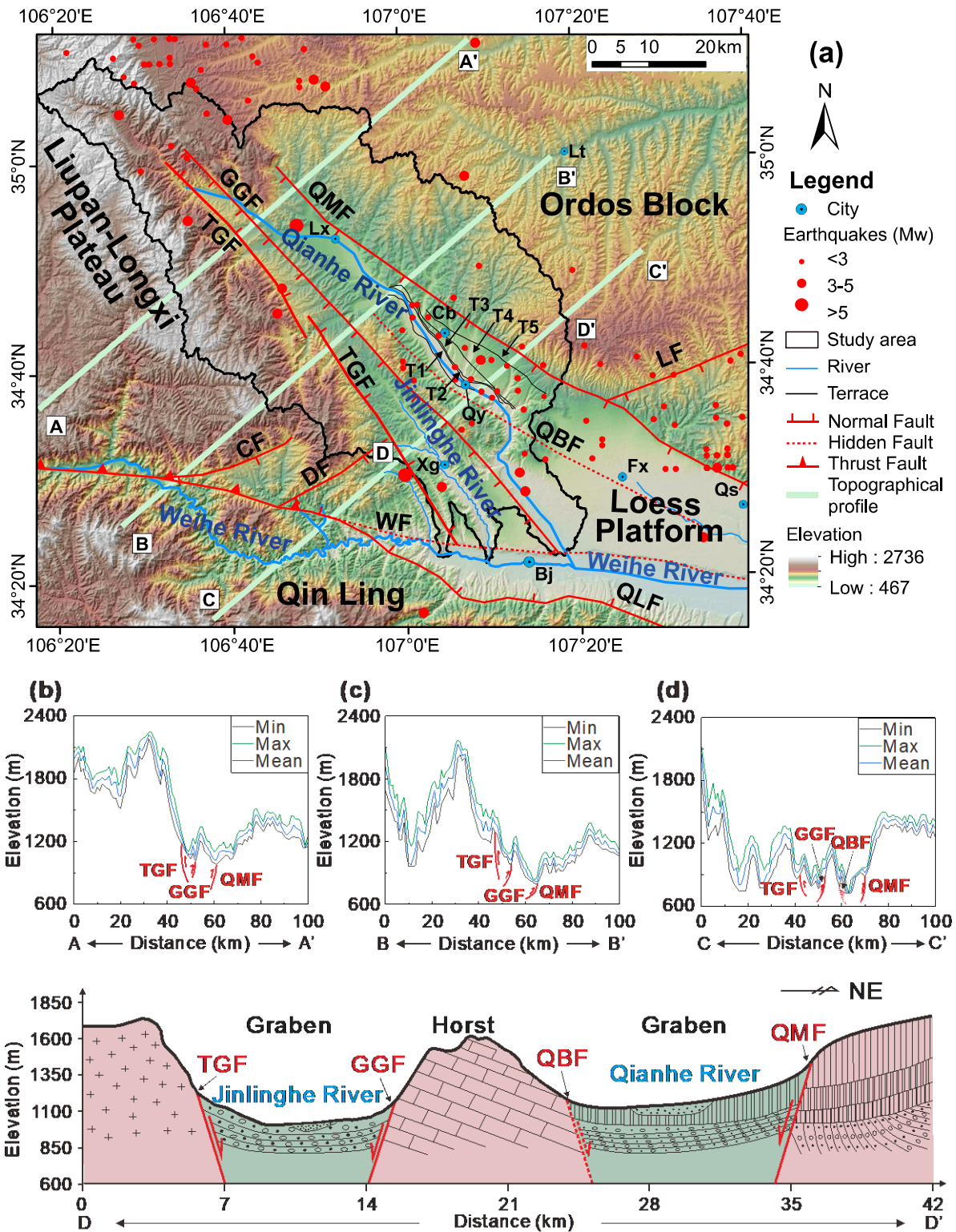


Fig. 2. Geomorphology of the study area. (a) SRTM (1 arc-second, NASA/USGS) was used as the digital elevation model of the Qianhe fault zone, the black terrace lines on the north side of Qianhe modified from (Chen et al., 2018b). Key cities: Lt, Liangting; Cb, Caobi; Qy, Qianyang; Qs, Qishan; Bj, Baoji; Fx, Fengxiang. LF, Linyou Fault; CF, Chishazhen Fault; DF, Duijiashan Fault; QLF, Qinling Fault; WF, Weihe Fault. (b) ~ (d) The topographical profiles of AA', BB', CC', respectively. (e) Tectonic framework modified from Shi (2011).

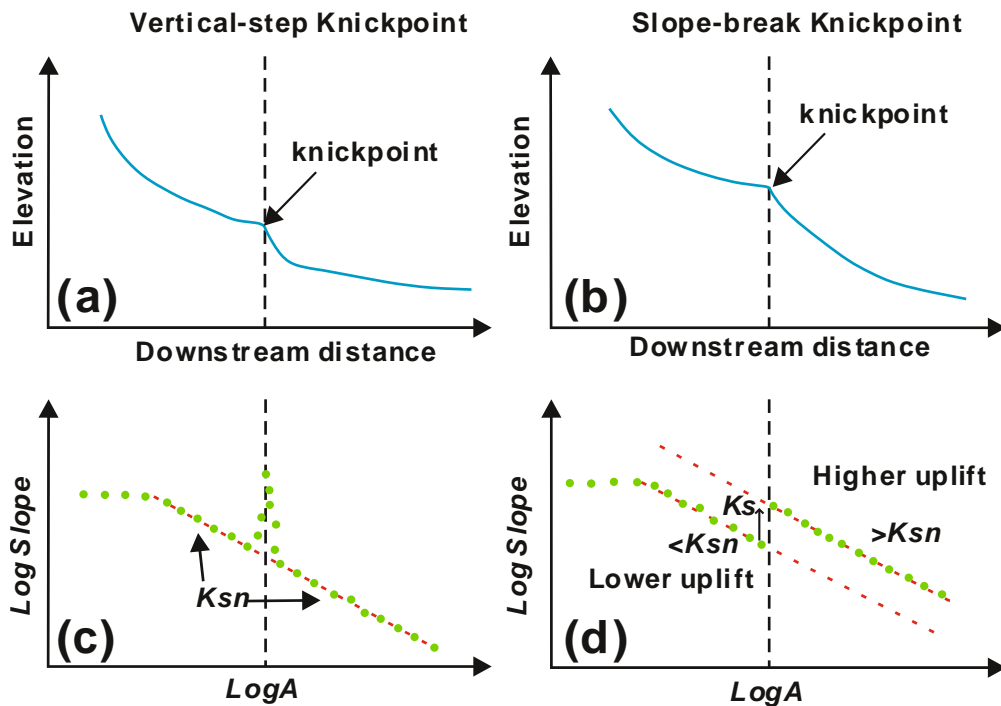


Fig. 3. Knickpoints patterns in terms of river longitudinal profile and log-log slope-area plot. Both morphologies may represent the fluvial response to active faults, modified from Kirby and Whipple (2012).

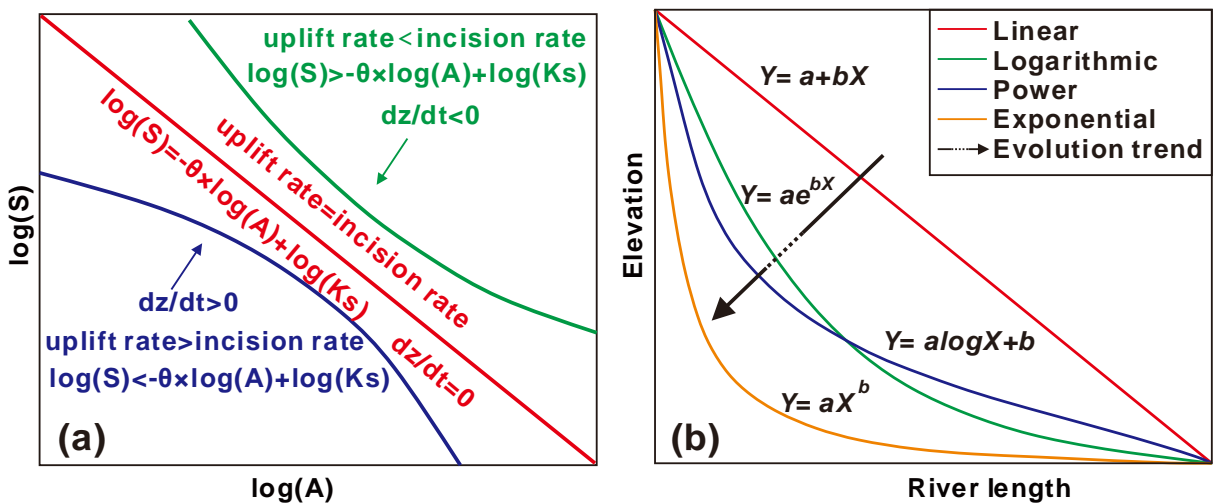


Fig. 4. (a) Standard logarithmic S-A plot of stream-power incision model, modified from (Chen et al., 2006); (b) Fit to the river profile by mathematic models. Where Y is elevation; X is the length of the river, a , b are coefficients independently determined for each profile, modified from Dong et al. (2017).

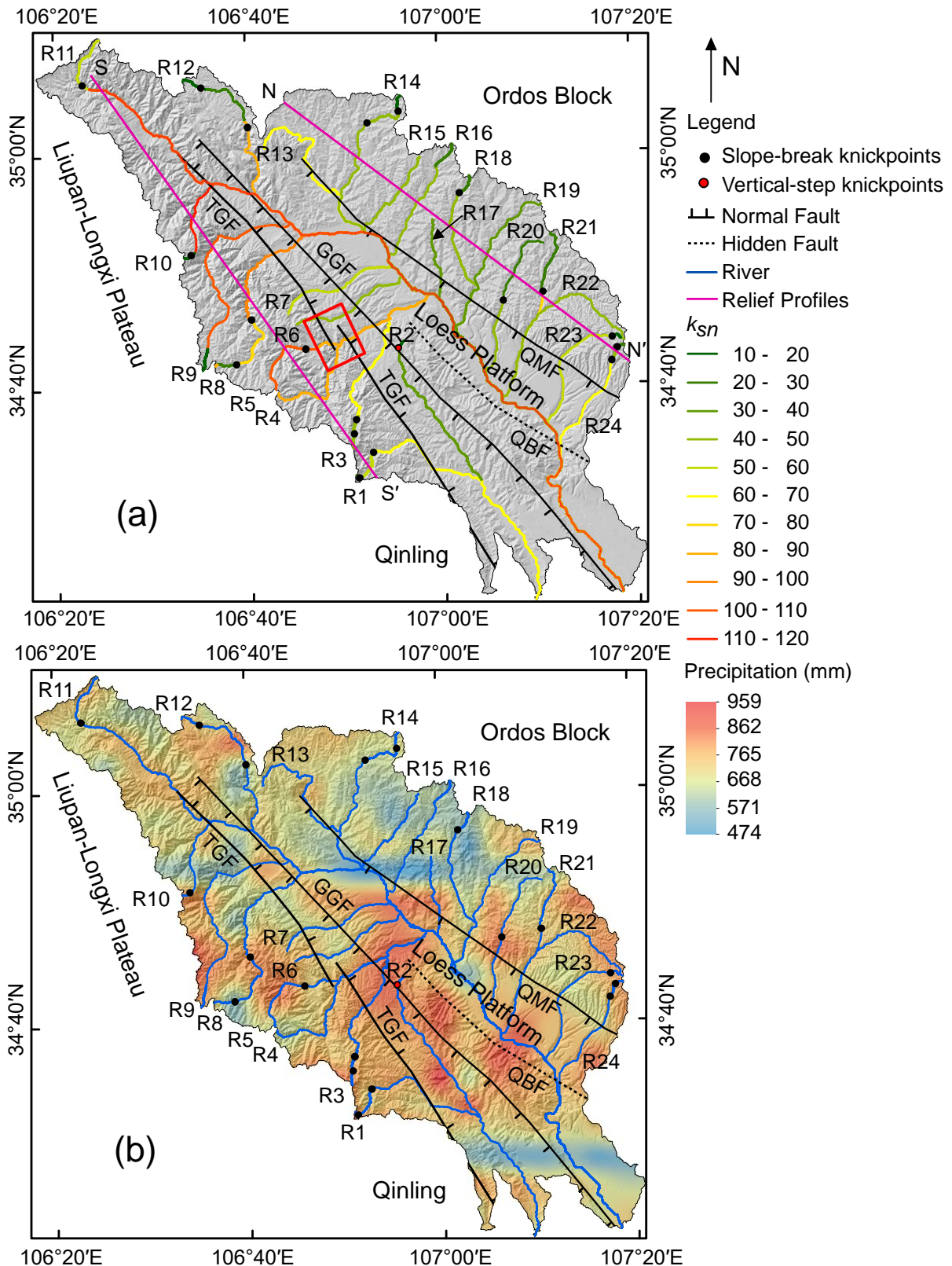


Fig. 5. (a) The distribution of main rivers and knickpoints in study area. The black points are the slope-break knickpoints and the red point is the vertical-step knickpoint. River 1 to River 11 are south rivers, River 12 to River 24 are north rivers. The red box indicates the location of potential fault linkage in the future. NN' and SS' are two profiles along the strike and paralleling the QMF and TGF. (b) Annual mean

precipitation distribution map in 2017, resampled from PERSIANN-Cloud Classification System (PERSIANN-CCS). See Fig. 1 for fault names.

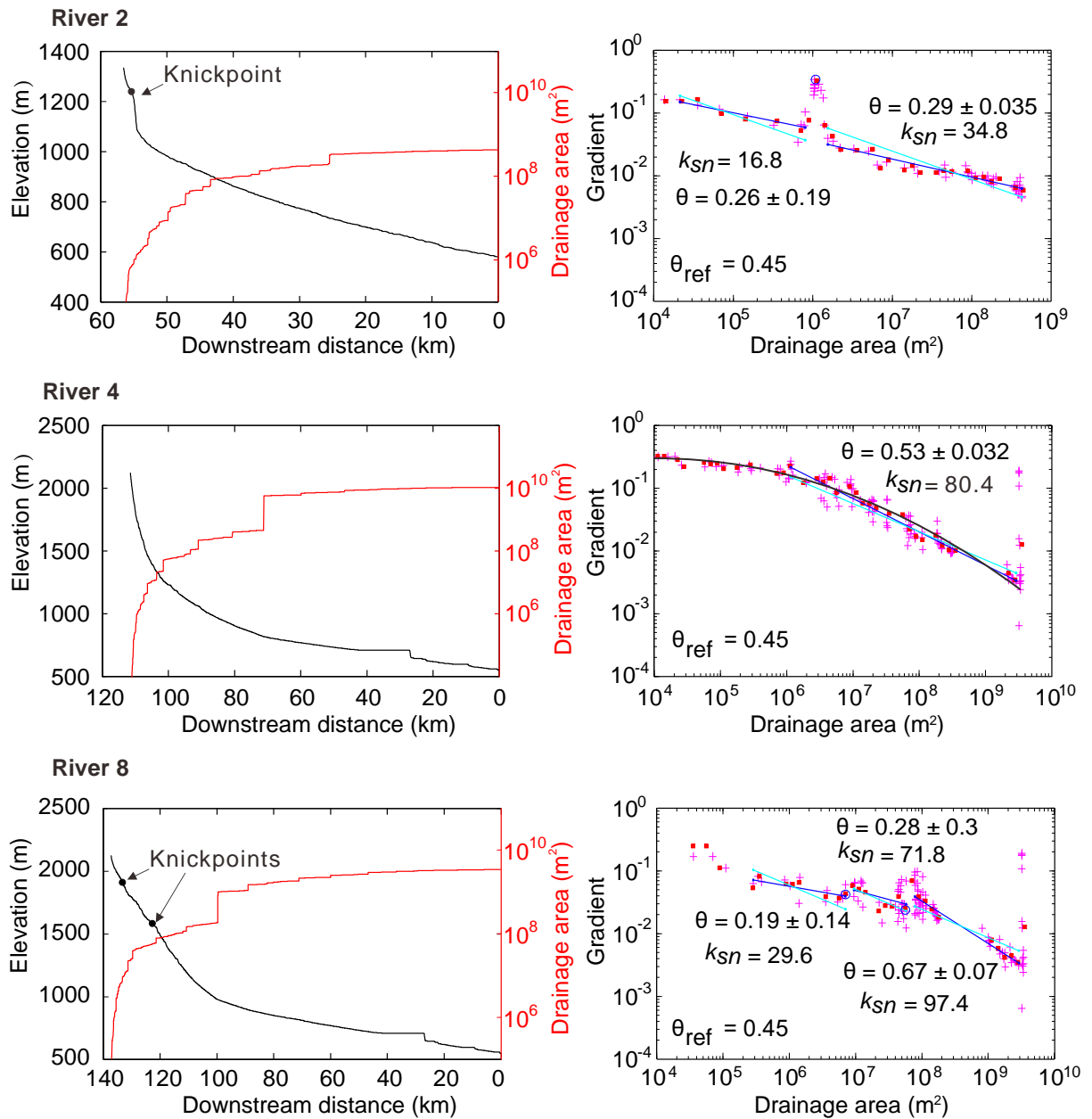


Fig. 6. The left columns show representative examples of river longitudinal profiles (black solid lines), the relationship between downstream distance and drainage area (red solid lines), and black points mark the knickpoints location. While the right columns show the SA plots extracted from SRTM1, and the concavities, θ , and normalised steepness index, k_{Sn} , where $\theta = 0.45$ are also shown on the SA plots. The black line on SA plot of River 4 is log(S) curve. All these rivers show different river longitudinal profiles with vertical-step knickpoints, without knickpoints, and slope-break knickpoints, respectively.

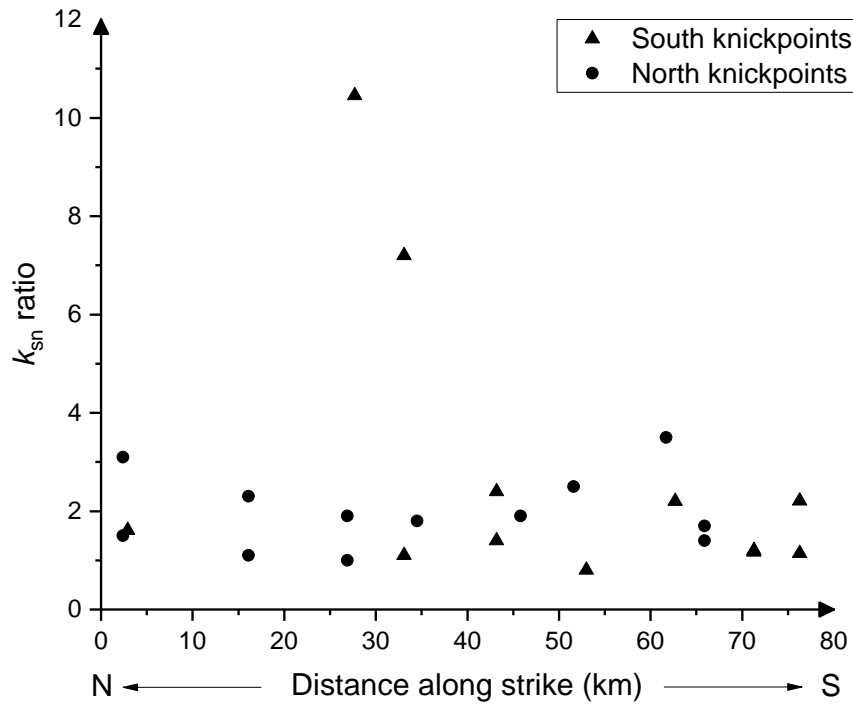


Fig. 7. The k_{sn} ratios of knickpoints along strike.

0

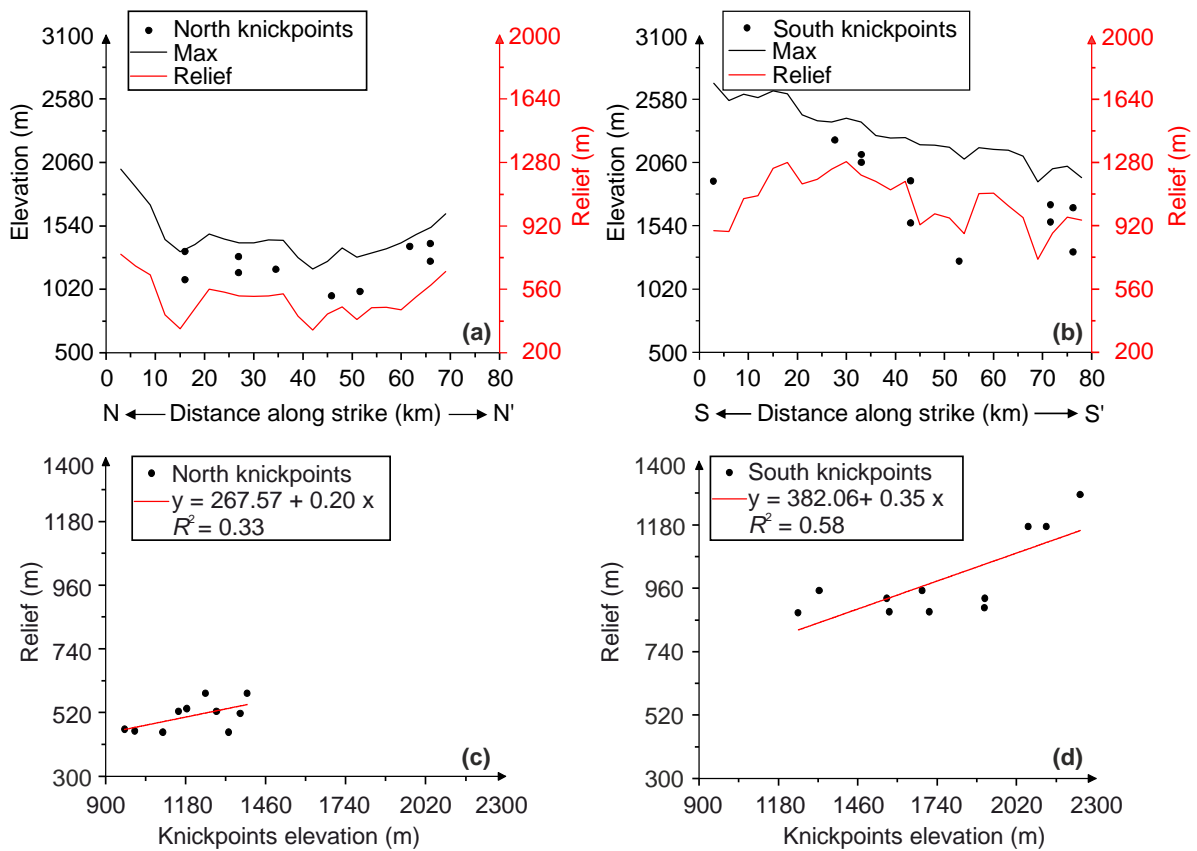


Fig. 8. The relationship between the elevation of the knickpoints and profile relief plotted along strike, which shows that there is a similar trend between the elevation of the knickpoints and relief. (a) and

(b) are the north and south profile relief along strike, respectively. (c) and (d) are the north and south profile (NN' and SS') relief against knickpoint elevation, respectively.

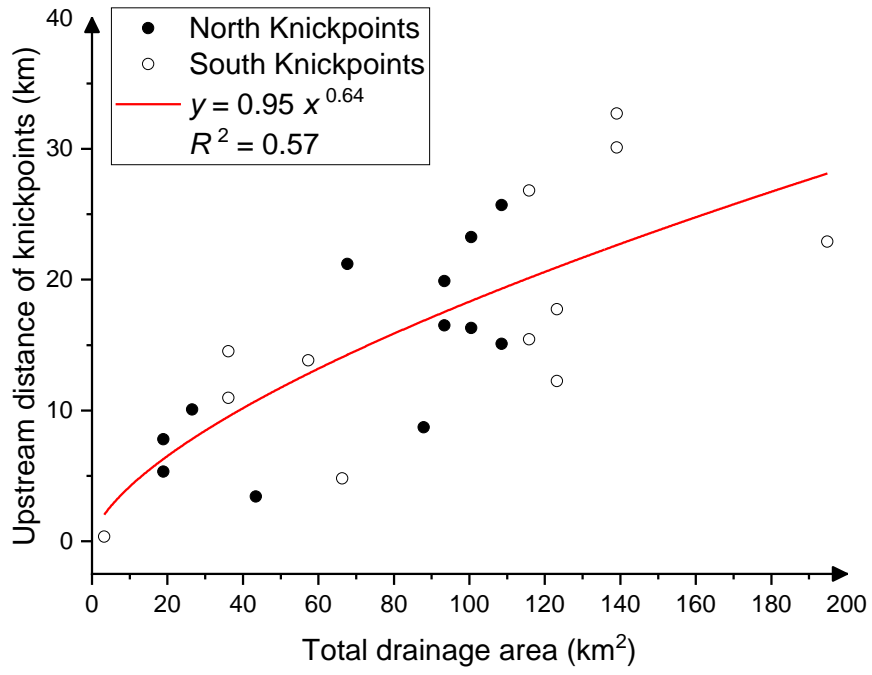


Fig. 9. The map of upstream distance from faults to knickpoints against total drainage area.

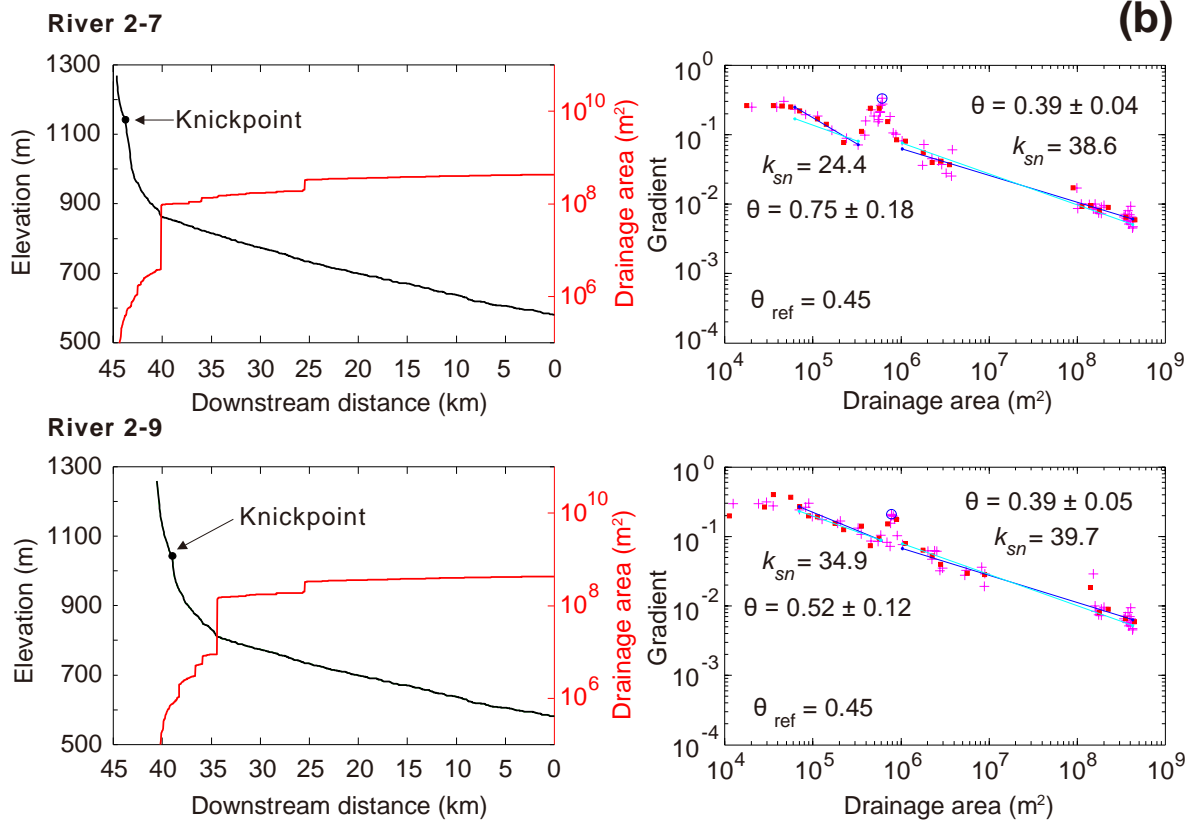
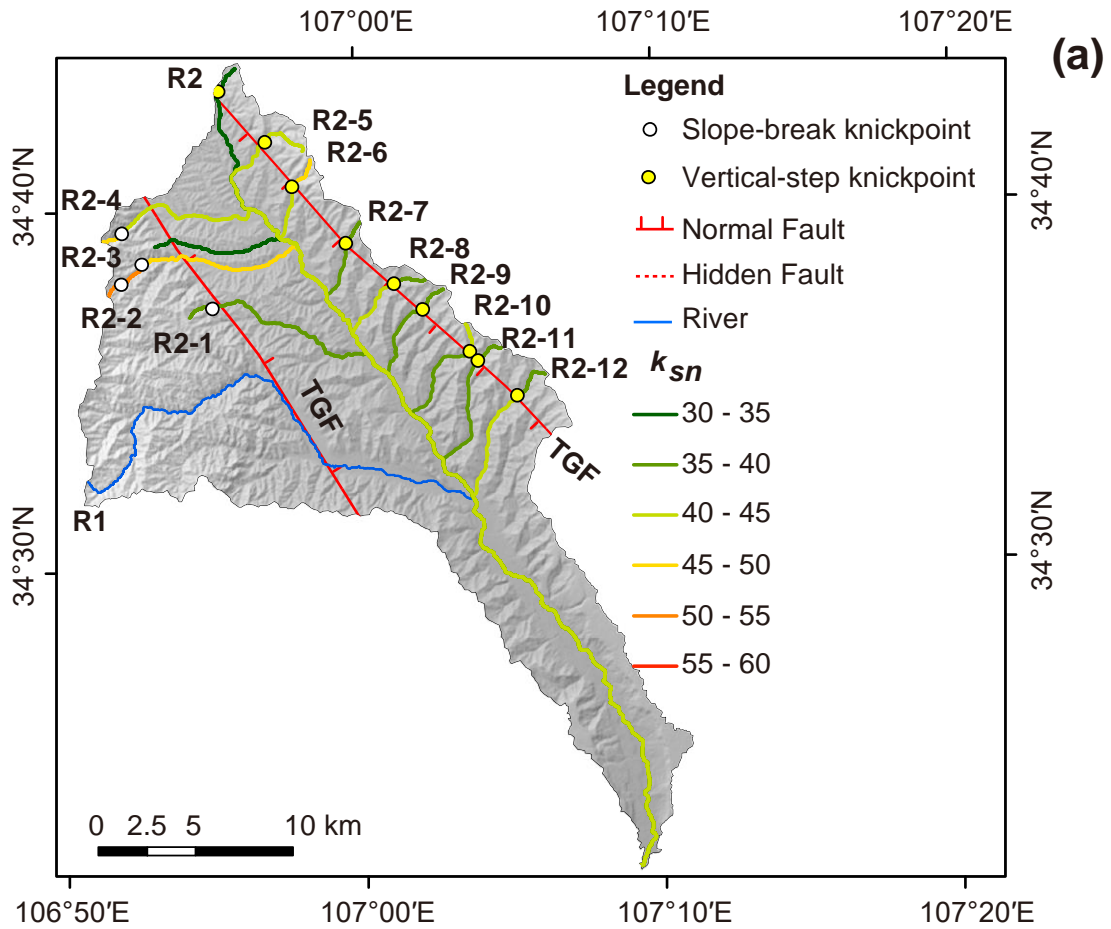


Fig. 10. (a) The topography map of Jinlinghe Graben. (b) Representative Slope-Area plots for two tributaries on northside of River 2.

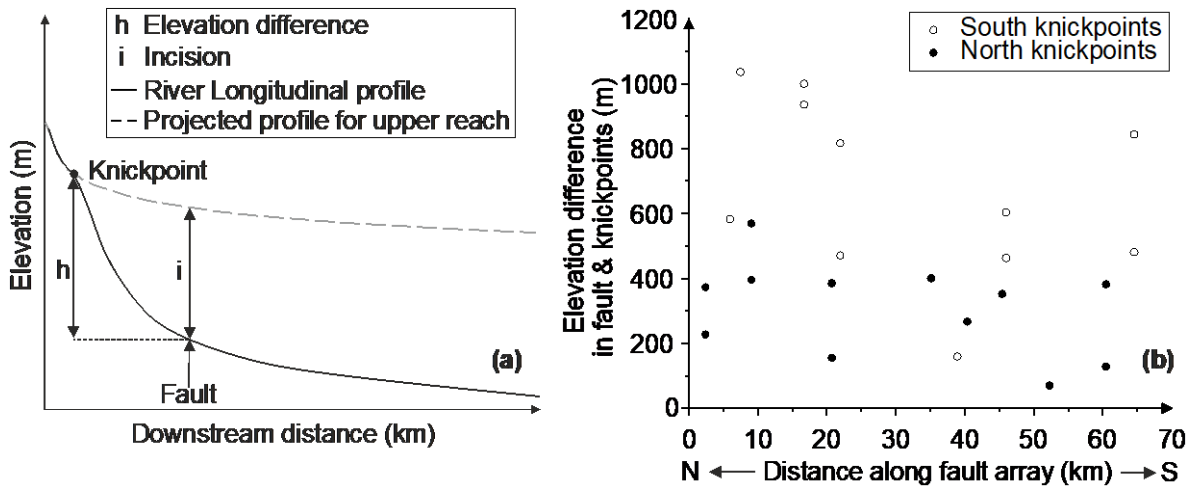


Fig. 11. (a) River longitudinal profile shows the difference between fault and knickpoints. The dashed line shows the projected profile for upper reach. (b) The elevation difference in fault and knickpoints of Qianhe Graben.

3

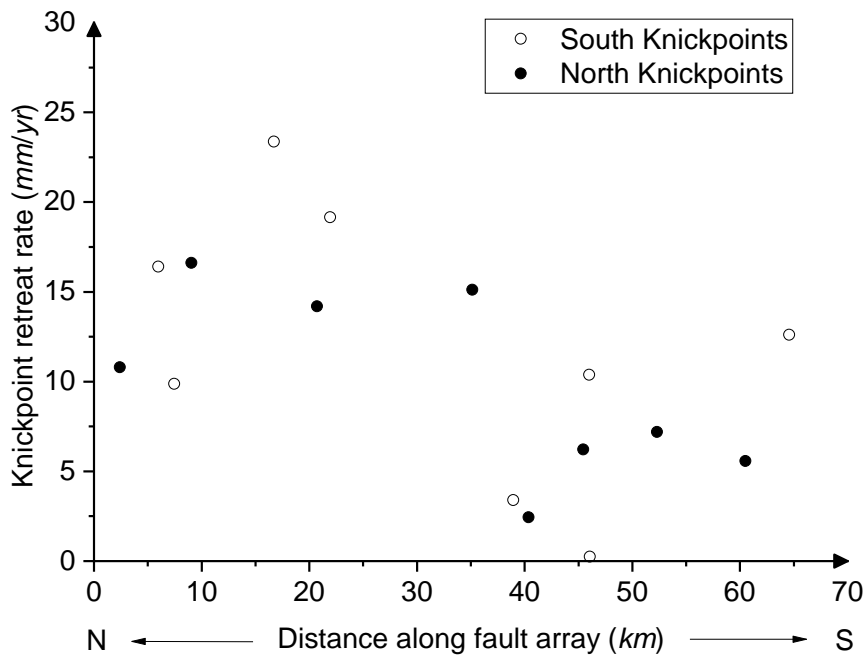


Fig. 12. Retreat rates of knickpoints (except for the lower knickpoints) along strike in this study area, showing a range of fault initiation at 1.4 Myr.

4

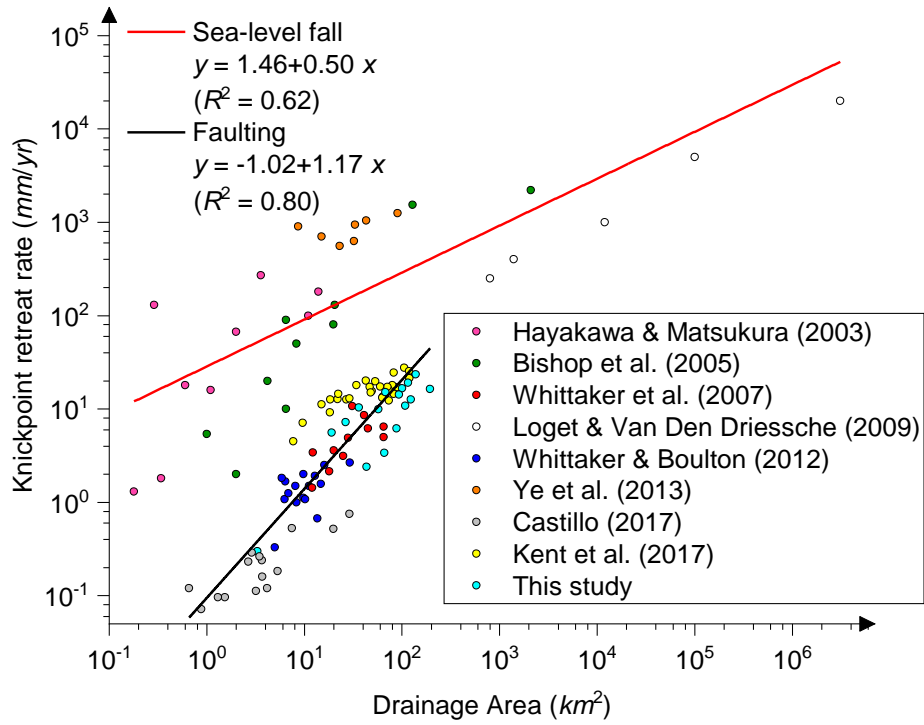


Fig. 13. The map of knickpoint retreat rates of knickpoints against drainage area in different areas. 1.4 Myr was selected as the age of the fault initiation in this study area (see text for details).

5

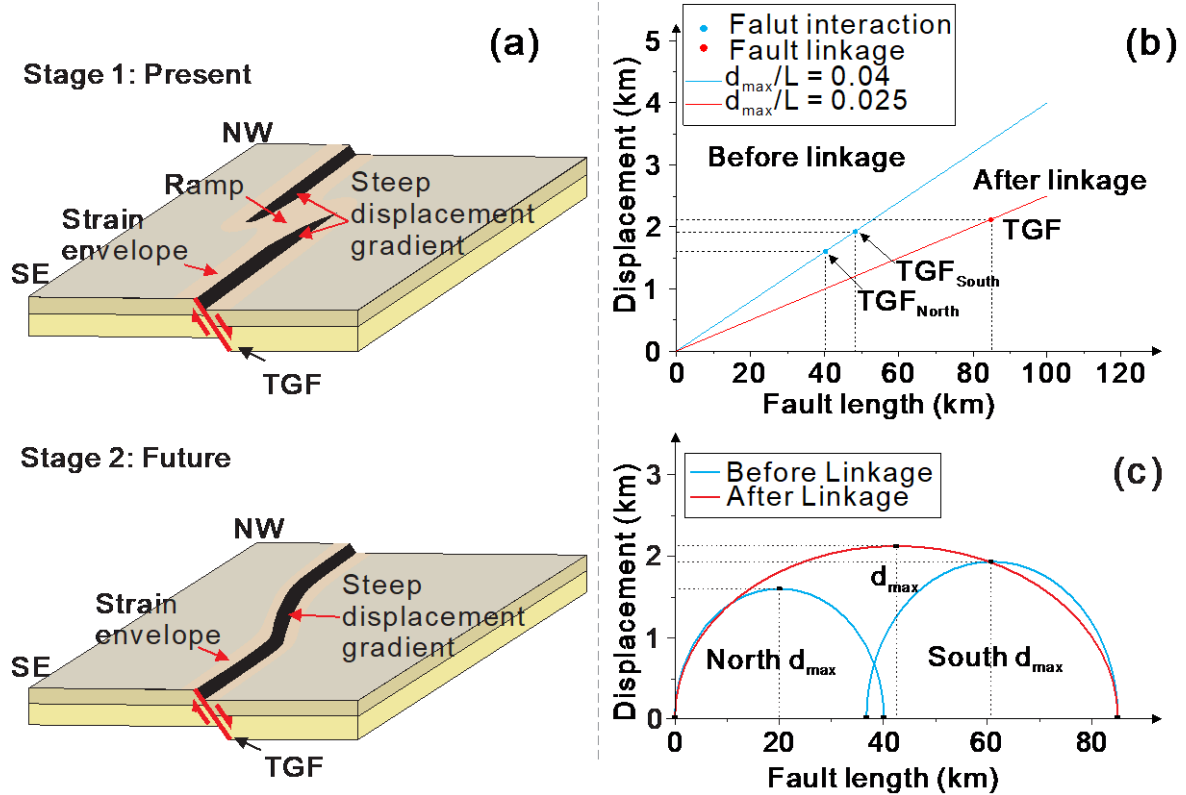


Fig. 14. (a) Plot of different states before and after fault linkage. (b) The relationship between faults length and displacement of TGF. (c) Fault linkage model (Wells and Coppersmith, 1994; Kim and Sanderson, 2005; Fossen and Rotevatn, 2016; Wang et al., 2018a).

Table 1. The statistics of extracted long rivers with knickpoints. * donates rivers with second (higher) knickpoints.

River Number	Distance along strike km	river length km	Relief m	Active fault elevation m	Total Drainage area km ²	Knickpoint elevation m	Upstream distance of knickpoints km	k_{sn} above knickpoint m ^{0.9}	k_{sn} below knickpoint m ^{0.9}	k_{sn} ratio	Knickpoint retreat rate (at 1.2 Myr) mm/yr	Knickpoint retreat rate (at 1.4 Myr) mm/yr
1*	76.3	54.9	952	843	123.2	1687	17.7	26.8	59.2	2.2	14.8	12.6
						1324	12.2	59.2	67.2	1.1	10.2	8.7
2	62.7	56.3	1033	1076	3.3	1119	0.4	16.8	34.8	2.1	0.3	0.3
3*	71.3	108.8	878	1109	36.2	1713	14.5	42.1	49.1	1.2	12.1	10.4
						1572	11.0	49.1	62.5	1.2	9.2	7.9
5	53.0	109.3	875	1091	66.3	1250	4.8	101.0	84.3	0.8	4.0	3.4
8*	43.2	137.2	925	1092	115.8	1909	26.8	29.6	71.8	2.4	22.3	19.1
						1562	15.4	71.8	97.4	1.4	12.8	11.0
9*	33.1	143.9	1174	1125	139.1	2125	32.7	12.9	14.7	1.1	27.3	23.4
						2061	30.1	14.7	106.0	7.2	25.1	21.5
10	27.7	134.5	1285	1209	57.3	2245	13.8	11.0	115.0	10.5	11.5	9.9
11	2.9	160.1	892	1324	194.9	1907	22.9	56.6	91.0	1.6	19.1	16.4
12*	2.4	111.0	760	1151	108.6	1720	15.1	18.6	28.0	1.5	12.6	10.8
						1546	25.7	28.0	88.1	3.1	21.4	18.4
14*	16.1	123.3	452	945	100.5	1330	23.3	20.0	43.1	2.3	19.4	16.6
						1100	16.3	43.1	45.8	1.1	13.6	11.6
16*	26.9	106.7	524	888	93.4	1288	19.9	23.7	24.6	1.0	16.6	14.2
						1155	16.5	24.6	46.8	1.9	13.8	11.8
18	34.5	93.2	534	832	67.7	1184	21.2	24.3	43.1	1.8	17.7	15.1
20	45.8	80.2	462	897	43.4	966	3.4	22.7	43.8	1.9	2.8	2.4
21	51.6	79.0		874	87.9	1002	8.7	28.6	70.8	2.5	7.3	6.2
23	61.7	61.0	517	989	26.6	1371	10.1	17.2	59.3	3.5	8.4	7.2
24*	65.9	54.6	586	1023	19.0	1395	7.8	27.5	46.7	1.7	6.5	5.6
						1250	5.3	46.7	65.7	1.4	4.4	3.8

Table 2. The information about long river profiles without knickpoints.

No	Length (km)	Log(S) Curve	k_{sn}	θ	\pm	R^2			
						Linear	Exponential	Logarithmic	Power
4	111.4	Convex	80.4	0.53	0.03	0.76	0.84	0.97	0.89
6	99.5	Linear	46.6	0.43	0.03	0.74	0.80	0.95	0.93
7	102.0	Linear	50.3	0.32	0.07	0.78	0.83	0.95	0.92
13	78.6	Convex	60.7	0.55	0.05	0.74	0.81	0.95	0.92
15	106.7	Convex	43.2	0.37	0.03	0.86	0.90	0.93	0.88
17	83.6	Linear	30.1	0.37	0.04	0.87	0.90	0.90	0.88
19	63.1	Linear	36.3	0.38	0.03	0.83	0.88	0.90	0.87
22	83.7	linear	45.9	0.26	0.04	0.85	0.92	0.93	0.83

8

Table 3. The statistics of the vertical-step knickpoints in the River 2 tributaries.

River number	River length (km)	k_{sn} above knickpoints	k_{sn} below knickpoints	k_{sn} ratio
R2-5	55.2	40.2	39.4	1.0
R2-6	49.4	49.9	40.8	0.8
R2-7	44.7	24.4	38.6	1.6
R2-8	42.9	29.2	40.4	1.4
R2-9	40.5	34.9	39.7	1.1
R2-10	38.6	33.0	39.1	1.2
R2-11	36.4	27.6	39.7	1.4
R2-12	34.4	26.7	42.0	1.6

9

Table 4. Statistics of knickpoints retreat rates (mm/yr) between the two sides of Qianhe Graben.

Fault	Maximum		Minimum		Mean	
	at 1.4 Myr	at 1.2 Myr	at 1.4 Myr	at 1.2 Myr	at 1.4 Myr	at 1.2 Myr
TGF	23.4	27.3	0.3	0.3	12.1	14.1
QMF	16.6	19.4	2.4	2.8	10.3	12.0

10